

**FACULTY
OF MATHEMATICS
AND PHYSICS**
Charles University

MASTER THESIS

Bc. Daniel Chmúrny

**Kernel integrals in time–distance
helioseismology**

Astronomical Institute of Charles University

Supervisor of the master thesis: doc. Mgr. Michal Švanda, Ph.D.

Study programme: Physics

Study branch: Astronomy and Astrophysics

Prague 2024

I declare that I carried out this master thesis independently, and only with the cited sources, literature and other professional sources. It has not been used to obtain another or the same degree.

I understand that my work relates to the rights and obligations under the Act No. 121/2000 Sb., the Copyright Act, as amended, in particular the fact that the Charles University has the right to conclude a license agreement on the use of this work as a school work pursuant to Section 60 subsection 1 of the Copyright Act.

In date

Author's signature

I would like to express my gratitude to my supervisor, doc. Mgr. Michal Švanda, Ph.D., for his exceptional guidance through the work on this thesis and endless patience during hours of consultations and hundreds of exchanged e-mails (this is not a hyperbole). I would also like to thank my wife, Olesia, for always helping me to pursue my goals when I lacked the will to do so myself.

Title: Kernel integrals in time–distance helioseismology

Author: Bc. Daniel Chmúrny

Institute: Astronomical Institute of Charles University

Supervisor: doc. Mgr. Michal Švanda, Ph.D., Astronomical Institute of Charles University

Abstract: This thesis presents a model-independent method for evaluating the volume integrals of velocity perturbation sensitivity kernels using helioseismic travel-time measurements. By injecting a controlled longitudinal flow into Dopplergram datacubes and analyzing the resultant travel-time perturbations, this study establishes a reliable approach to obtain kernel integrals independently of theoretical models. These are then compared to their counterparts calculated from forward modelling. The method showed strong correlation with model kernels for ridge filters, f and $p1 - p4$. On the other hand, strong inconsistencies were observed for phase speed filters, $td1 - td11$, showing almost no correlation with model kernels. These results suggest yet unidentified issues in kernel calculation methods employed by various models.

Keywords: time-distance, helioseismology, sensitivity kernels

Název práce: Integrované kernelů pro time–distance helioseismologii

Autor: Bc. Daniel Chmúrny

Katedra: Astronomický ústav Univerzity Karlovy

Vedoucí práce: doc. Mgr. Michal Švanda, Ph.D., Astronomický ústav Univerzity Karlovy

Abstrakt: Tato práce představuje modelově nezávislou metodu testování objemových integrálů citlivostních jader pro perturbace rychlostí pomocí měření cestovních časů helioseismických vln. Vkládáním kontrolovaného zonálního toku do datových kostek složených z Dopplergramů a analýzou výsledných perturbací cestovních časů se studie snaží zavést spolehlivý přístup k získání integrálů citlivostních jader nezávisle na teoretických modelech. Ty jsou poté porovnány s jejich protějšky vypočtenými z forward modelů. Metoda prokázala silnou korelaci s modelovými jádry pro tzv. hřebínkové filtry, f a $p1 - p4$. Na druhou stranu byly pozorovány výrazné nesrovnalosti pro filtry konstantní fázové rychlosti, $td1 - td11$, vykazujícími téměř nulovou korelaci s modelovými citlivostními jádry. Tyto výsledky poukazují na dosud neidentifikované problémy v metodách výpočtů citlivostních jader.

Klíčová slova: time-distance, helioseismologie, citlivostní jádra

Contents

Introduction	3
1 Solar structure	4
1.1 Core	4
1.2 Radiative zone	5
1.3 Tachocline	5
1.4 Convective zone	5
1.5 Photosphere	6
2 Solar oscillations	7
2.1 Basic hydrodynamic equations	7
2.2 Internal waves	9
2.2.1 Acoustic waves (p modes)	10
2.2.2 Gravity waves (g modes)	10
2.2.3 Surface gravity waves (f modes)	11
2.3 Observations	12
3 Helioseismology	15
3.1 Local helioseismology	15
3.2 Time-distance helioseismology	16
3.2.1 Travel times	18
3.2.2 Travel-time sensitivity kernels	20
4 Methodology	22
5 Data analysis	24
5.1 Source of Data - SDO/HMI	24
5.2 HMI Dopplergrams	25
5.3 Azimuthal equidistant (Postel) projection	28
5.4 Tracking pipeline	29
5.5 Travel-time pipeline	36
6 Results	38
7 Discussion	51
7.1 Injected velocity flow vs. real flow	51
7.2 Observation times	53
7.3 GB02 vs. GB04	53
7.4 Differential rotation	54
7.5 Reference cross-covariance	54
Conclusion	55
Bibliography	56
List of Figures	60

List of Tables	63
List of Abbreviations	64

Introduction

Blazing in gold and quenching in
purple,
Leaping like leopards to the sky,
Then at the feet of the old horizon
Laying her spotted face, to die;

Stooping as low as the otter's
window,
Touching the roof and tinting the
barn,
Kissing her bonnet to the
meadow, —
And the juggler of day is gone!

The Juggler of Day
Emily Dickinson

The Sun, the closest star to planet Earth and the center of our planetary system, is a star that appears blatantly unremarkable in almost every measurable aspect, yet it holds immense significance for every single living organism, including us, humans. From providing suitable conditions for life to offering one of the earliest methods to measure time, our home star has been our closest ally for millennia. It is, therefore, somewhat ironic that for the vast majority of our history as a species, we knew virtually nothing about it.

The first true astronomical observations, and thus the first pieces of actual knowledge, can be attributed to the ancient Chinese for their observations of sunspots (Xu Zhen-tao, 1980). Similar measurements were later conducted by Arabs, Europeans, and others, as described in Vaquero (2007). While sunspots continue to serve as useful markers of solar activity even today, they do not reveal much about the inner structure of the Sun. This limitation, the inability to see below the optically thick photosphere, remained a challenge until only very recently. It was only after the discovery of the "5-minute oscillations" in the 1960s (Leighton et al., 1962) and their theoretical explanation in the 1970s (Ulrich, 1970; Leibacher and Stein, 1971) that we were finally able to peek deeper beneath the "surface" and expand our knowledge about the Sun far beyond just its visible disc.

The field of astrophysics that has enabled these deeper insights is called helioseismology, often referred to as one of the most successful branches of astrophysics (Buldgen, 2019). Helioseismology fundamentally involves the analysis of acoustic wave propagation within the Sun. Despite its success and valuable contributions, helioseismology remains a relatively young and evolving field of physics, and some of its concepts and fundamental quantities have not yet been fully proven or tested. Among these are the *sensitivity kernels*, which analytically computed from various models, indicate how much various perturbations within the Sun's interior influence observable properties at its surface. The aim of this thesis is to develop a model-independent method to verify the accuracy of at least one of these sensitivity kernels.

1. Solar structure

The Sun is a main sequence star of stellar classification G2V located in a disc of the Milky Way galaxy, approximately 8 kpc from its center. Its interior structure can be divided into four main regions; the core, the radiative zone, the convective zone and the photosphere as shown in more detail in Fig. 1.1.

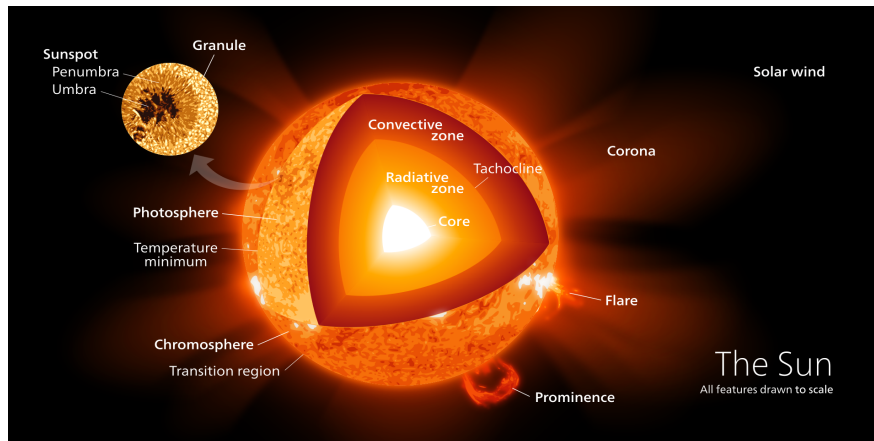


Figure 1.1: The interior structure of the Sun. Credit: Wikipedia Commons/kelvinsong

1.1 Core

The core constitutes the innermost layer of the Sun, extending from its center to approximately 20–25 % of its radius R_{\odot} (García et al., 2007; Hathaway, D. H., 2022). Within this region, hydrogen nuclei undergo fusion to form helium through the proton-proton chain (Salpeter, 1952), a process known as thermonuclear fusion. This reaction releases a substantial amount of energy, approximately 6.7 MeV per nucleon (Schumacher, 2001), which is subsequently emitted from the Sun’s photosphere as visible light. Achieving conditions conducive to nuclear fusion is no trivial matter, as emphasized by Schumacher (2001). The reaction is particularly sensitive to temperature and density. The solar core maintains a central temperature of approximately 15×10^6 K and a density of about 150×10^3 kg/m³ (Hathaway, D. H., 2022). By around 20–25 % of the solar radius, the temperature decreases to about half its central value, while the density drops to less than $\frac{1}{6}$ of its initial magnitude. At this juncture, the temperature and pressure become insufficient to sustain nuclear fusion, marking the boundary between the solar core and the surrounding layers.

1.2 Radiative zone

Above the boundary of the core lies the radiative zone, extending further up to approximately 70 % of the Sun’s radius. Its nomenclature derives from the predominant mode of energy transport within it: radiation. Due to its considerable volume and high optical thickness, it takes approximately a million years for a photon emitted in the core to traverse the radiative zone and reach the tachocline. The temperature and density gradually decline to approximately 2×10^6 K and 200 kg/m^3 , respectively, at the upper boundary (Hathaway, D. H., 2022). Moreover, as demonstrated by Bro (1985) and Howe (2009), the radiative zone exhibits a rotational behavior akin to that of a rigid body, displaying minimal evidence of differential rotation—a phenomenon contrasting sharply with the convective zone situated above it.

1.3 Tachocline

The tachocline serves as a transitional region between the radiative zone and the convective zone, exhibiting fundamental differences not only in terms of energy transport mechanisms but also in their rotational dynamics. Whereas the radiative zone demonstrates an almost rigid body rotation, the convective zone undergoes differential rotation. Given its approximate thickness of only $0.002 R_{\odot}$ (as per Elliott and Gough, 1999; Rogers, 2011), the tachocline experiences rapid changes in its rotation profile, causing significant shear within the layer.

Some researchers (e.g. Gilman, 2005)) have proposed that the tachocline may play a pivotal role in the solar dynamo process and potentially contribute to the formation of magnetic patterns observable in the photosphere. Conversely, findings by Wright and Drake (2016) suggest that the tachocline’s significance for these phenomena may be considerably less than anticipated, if indeed present at all.

1.4 Convective zone

The convective zone extends from the upper boundary of the tachocline, situated approximately at $0.715 R_{\odot}$ (Christensen-Dalsgaard et al., 1991; Schumacher and Sreenivasan, 2020), to the near surface. In this region, the temperature and density are insufficient for energy to be transferred via radiation. However, the relatively low density permits the occurrence of convective currents, allowing for the transfer of energy from the lower layers to the surface.

Convection within the convective zone is propelled by a steep temperature gradient where the plasma near the tachocline undergoes heating and expansion, consequently decreasing its density and causing it to ascend. This upward movement of heated plasma results in a continuous circulation pattern, with cooler material descending to replace the rising warm plasma.

The convective motion effectively transports energy outward, ultimately contributing to the surface phenomena observed in the Sun (Schumacher and Sreenivasan, 2020). Such phenomena mainly include granulation and super-granulation (Leighton, 1963; Hathaway, D. H., 2022) which cause the familiar granular structure in observation of the solar photosphere as can be seen in Fig. 1.2.

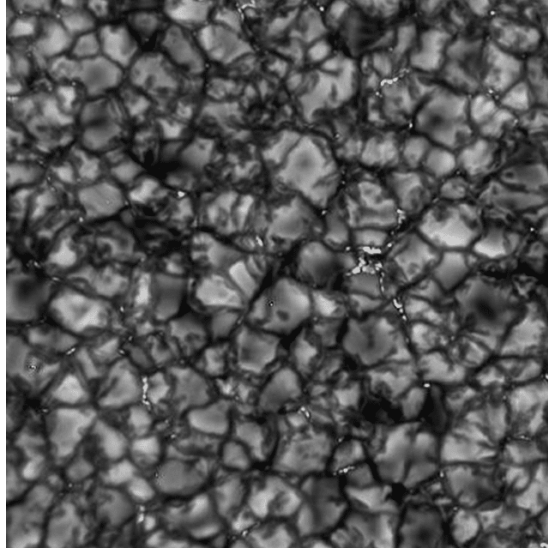


Figure 1.2: Closeup image of granulation in solar photosphere. Credit: NSO (nso.edu).

1.5 Photosphere

The photosphere, the Sun's visible surface, plays a crucial role in solar observation, offering insights into its activities. It extends from the top of the convective zone up about 100 km where it blends into chromosphere (Hathaway, D. H., 2022). With temperatures ranging between 4,000 and 6,500 K, the photosphere emits light across the visible spectrum, allowing for direct observation. This emitted light primarily originates from the convective zone, where energy initially created in the core rises upward.

Distinctive patterns like granules and super-granules are present in the photosphere. Granules, small bright cells approximately 1,000 kilometers wide, form as hot plasma rises and cools. Super-granules, larger networks of these cells up to 30,000 kilometers wide, reveal the underlying convective processes (Leighton, 1963; Hathaway, D. H., 2022).

Transient events such as sunspots, faculae, and solar flares are also observable in the photosphere. Sunspots, dark patches resulting from intense magnetic activity, and faculae, bright spots indicating active magnetic regions, provide valuable insights into magnetic field dynamics (Hathaway, D. H., 2022).

2. Solar oscillations

2.1 Basic hydrodynamic equations

This subsection aims to introduce a simple model for solar oscillations, derived from basic hydrodynamic equations. Some technical steps are omitted from the derivation to enhance clarity, but more detailed explanations, including all technical steps, can be found in the works of Kosovichev (2011), Christensen-Dalsgaard (2002), and Korda (2020).

We commence by assuming the following (Kosovichev, 2011; Korda, 2020):

1. oscillation velocities \mathbf{v} are much smaller than the sound speed c_s , i.e. $\frac{v}{c_s} \ll 1$
2. adiabatic approximation
3. spherical symmetry
4. negligible magnetic forces and stresses

Then the set of governing equations consists of the equation of continuity representing a conservation of mass, Euler's equation (equation of motion), adiabaticity equation and Poisson equation, written in this order:

$$\frac{\partial \rho}{\partial t} + \nabla \cdot (\rho \mathbf{v}) = 0, \quad (2.1a)$$

$$\rho \frac{d\mathbf{v}}{dt} = -\nabla \cdot P - \rho \mathbf{g}, \quad (2.1b)$$

$$\frac{dP}{dt} = c_s^2 \frac{d\rho}{dt}, \quad (2.1c)$$

$$\Delta \Phi = 4\pi G \rho, \quad (2.1d)$$

where $\rho(\mathbf{r}, t)$ is a local density, $\mathbf{v}(\mathbf{r}, t)$ local material velocity, $P(\mathbf{r}, t)$ local pressure and Φ gravitational potential. The gravity acceleration \mathbf{g} can be expressed as a gradient of the gravitational potential, i.e. $\mathbf{g} = \nabla \Phi$. For the total time derivative of the material velocity vector, it holds that $\frac{d\mathbf{v}}{dt} = \frac{\partial \mathbf{v}}{\partial t} + \mathbf{v} \cdot \nabla \mathbf{v}$.

We consider small perturbations of velocity, density, and pressure from their initial values corresponding to a spherically symmetrical star in hydrostatic equilibrium: $v_0 = 0$, $\rho = \rho_o(r)$ and $P = P_0(r)$. Furthermore, we define a displacement vector $\boldsymbol{\xi}(t)$ defined

$$\mathbf{v} = \frac{d\boldsymbol{\xi}}{dt} \approx \frac{\partial \boldsymbol{\xi}}{\partial t} \quad (2.2)$$

Equations are further simplified by applying the so-called Cowling approximation, which presumes that perturbations of the gravitational potential contribute only minimally to the corrections of the theoretical oscillation frequencies and can thus be neglected. Furthermore, the equations are expressed in spherical coordinates and linearized. We encourage the reader to refer to Kosovichev (2011); Korda (2020); Christensen-Dalsgaard (2002) for a more detailed explanation of these steps.

The final set of linearized equations is as follows:

$$\rho' + \frac{1}{r^2} \frac{\partial}{\partial r} (r^2 \rho \xi_r) + \frac{\rho}{r} \nabla_h \xi_h = 0, \quad (2.3a)$$

$$-\omega^2 \rho \xi_r = -\frac{\partial P'}{\partial r} + g \rho', \quad (2.3b)$$

$$-\omega^2 \rho \xi_h = -\frac{1}{r} \nabla_h P', \quad (2.3c)$$

$$\rho' = \frac{1}{c_s^2} P' + \frac{\rho N^2}{g} \xi_r, \quad (2.3d)$$

where

$$N^2 = g \left(\frac{1}{\gamma P} \frac{dP}{dr} - \frac{1}{\rho} \frac{d\rho}{dr} \right) \quad (2.4)$$

is the *Brünt-Väisälä* (*buoyancy*) *frequency*, representing the frequency at which a parcel of fluid would oscillate vertically when displaced from its equilibrium position, and ω is the angular frequency of the periodic perturbations, i.e. oscillations. Physical quantities marked by primes, e.g. P' , in equations 2.3a - 2.3d represent Eulerian perturbations of the said quantities, while their counterparts without apostrophes denote initial unperturbed values.

The following boundary conditions are assumed:

1. zero displacement in the center, i.e. $\xi(r=0) = 0$ (except the dipole modes)
2. the Lagrangian pressure perturbation at the surface is zero, i.e. $\delta P(r=0) = 0$
3. the solution is regular at the Sun's center ($r=0$)
4. the solution is regular at the poles $\theta = 0, \pi$

A solution of Eqs 2.3a – 2.3d is searched for in a separated form:

$$\rho'(r, \theta, \phi) = \rho'(r) f(\theta, \phi), \quad (2.5a)$$

$$P'(r, \theta, \phi) = P'(r) f(\theta, \phi), \quad (2.5b)$$

$$\xi_r(r, \theta, \phi) = \xi_r(r)f(\theta, \phi), \quad (2.5c)$$

$$\boldsymbol{\xi}_h(r, \theta, \phi) = \xi_h(r)\boldsymbol{\nabla}_h f(\theta, \phi). \quad (2.5d)$$

A non-zero solution exists for $f(\theta, \phi)$ in a form of spherical harmonics $Y_l^m(\theta, \phi)$. This leads to a transformed set of hydrodynamic equations

$$\frac{d\xi_r}{dr} - \frac{g}{c_s^2}\xi_r + \left(1 - \frac{S_l^2}{\omega^2}\right) \frac{P'}{\rho c_s^2} = 0, \quad (2.6a)$$

$$\frac{dP'}{dr} + \frac{g}{c_s^2}P' + (N^2 - \omega^2)\rho\xi_r = 0, \quad (2.6b)$$

where $S_l^2 = \frac{l(l+1)c_s^2}{r^2}$ is the so-called *Lamb frequency*.

2.2 Internal waves

To derive a dispersion relation of the internal waves and their modes, we seek an oscillatory solution to equations 2.6 in the JWKB form:

$$\xi_r = A\rho^{-\frac{1}{2}}e^{ik_r r}, \quad (2.7a)$$

$$P' = B\rho^{\frac{1}{2}}e^{ik_r r}, \quad (2.7b)$$

where A and B are constants and k_r slowly varies with r . Then a general dispersion relation of internal waves can be found in a form (Kosovichev, 2011; Korda, 2020; Christensen-Dalsgaard, 2002):

$$k_r^2 = \frac{\omega^2 - \omega_c^2}{c_s^2} + \frac{S_l^2}{c_s^2\omega^2}(N^2 - \omega^2), \quad (2.8)$$

where

$$\omega_c = \frac{c_s}{2H_\rho} \quad (2.9)$$

is the *acoustic cut-off frequency* and

$$H_\rho = \left(\frac{d \ln \rho}{dr}\right)^{-1} \quad (2.10)$$

is called *density scale height*.

The waves can propagate only for cases when $k_r^2 > 0$. For $k_r^2 < 0$ the waves decay exponentially, these are called *evanescent waves*.

2.2.1 Acoustic waves (p modes)

Acoustic waves, also called p modes, can penetrate deep into the star, with their depth dependent on the Lamb frequency S_l . Modes with lower corresponding Lamb frequencies penetrate deeper, and vice versa. Unfortunately, the low S_l modes are challenging to detect due to their extended travel trajectory inside the star. Therefore, only waves penetrating no further than the convection zone are observable. An example of a p mode propagation is shown in Fig. 2.1.

It holds true for these waves that $\omega^2 \gg N^2$ which simplifies the general dispersion relation of internal waves, Eq. 2.8, into the form

$$\omega^2 = k^2 c_s^2 + \omega_c^2, \quad (2.11)$$

where $k^2 = k_r^2 + k_h^2$ and $k_h = \frac{\sqrt{l(l+1)}}{r}$.

The lower turning point r_{low} is determined by the relation $k_r = 0$. After substituting this relation into Eq. 2.11 we get the condition:

$$\omega^2 = \omega_c^2 + \frac{L^2 c_s^2}{r^2} = 0, \quad (2.12)$$

where $L^2 = l(l+1)$. The lower turning point is located inside of the Sun, typically in the convective zone, where $\omega \gg \omega_c$ and can be expressed implicitly as

$$r_{\text{low}} = \frac{L c_s(r_{\text{low}})}{\omega}. \quad (2.13)$$

The upper turning point r_{up} is bound to the cut-off frequency and exists where $\omega_c(r_{\text{up}}) \approx \omega$. The cut-off frequency ω_c rises very rapidly near the solar surface. Waves with $\omega < \omega_c$ are not able to react to changes in density and are reflected back into interior. Therefore, it can be assumed

$$r_{\text{up}} \approx R_{\odot} \quad (2.14)$$

2.2.2 Gravity waves (g modes)

Another type of wave is the so-called g mode, which propagates only in the inner parts of the Sun without penetrating into the convective zone as shown in an example in Fig. 2.1. G modes are low-frequency waves, so we can assume $\omega \ll S_l$ and the general dispersion relation 2.8 transforms into

$$\omega^2 = N^2 \cos^2 \theta, \quad (2.15)$$

where θ is an angle between \mathbf{k} and \mathbf{k}_h .

The condition of propagation for g modes is $\omega^2 \leq N^2$ with the lower turning point satisfies $\omega^2 \ll N^2$ in the depth

$$r_{\text{low}} = \frac{Lc_s(r_{\text{low}}) N(r_{\text{low}})}{\omega \omega_c(r_{\text{low}})}. \quad (2.16)$$

The upper turning point is where $k_r = 0$, which corresponds to the condition

$$\omega = N(r_{\text{low}}). \quad (2.17)$$

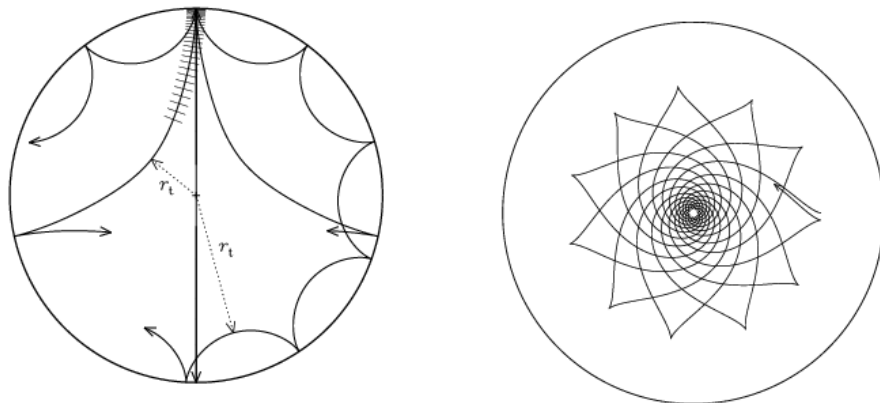


Figure 2.1: An illustration of a propagation of p modes (left) and g modes (right) in the Sun's interior. Credit: di Mauro (2016).

2.2.3 Surface gravity waves (f modes)

On the surface, similarly to the surface of deep water, we can observe surface gravity waves, or f modes. They are driven by buoyancy, and their propagation is limited to the surface boundary, where the Lagrangian pressure perturbation is approximately zero, i.e. $\delta P \sim 0$.

The dispersion relation of the f mode is thus very simple:

$$\omega^2 = k_h g = \frac{\sqrt{l(l+1)} GM_\odot}{R_\odot R_\odot^2}. \quad (2.18)$$

The f mode is diagnostically very important as it can be easily fitted in the power spectrum and Sun's density can be determined from the fit.

2.3 Observations

The propagation of various types of waves in helioseismology cannot be observed directly; instead, indirect methods are essential. Traveling waves affect plasma parameters, inducing phenomena such as local brightenings or Doppler shifts in photospheric spectral lines. These effects are pivotal for interpreting helioseismic waves, requiring a series of consecutive observations to understand their time evolution.

The standard input data for helioseismology comprises a time series of Dopplergrams (refer to Sec. 5.2). Although it's feasible to use time series of intensity measurements, Doppler velocities typically exhibit a higher signal-to-noise ratio, resulting in the common exclusion of intensity measurements.

At present, three primary sources of helioseismic data exist: the ground-based Global Oscillation Network Group (GONG) (Harvey et al., 1996), the Michelson Doppler Imager (MDI) (Scherrer et al., 1995) aboard the Solar and Heliospheric Observatory (SOHO) positioned at the L_1 Sun-Earth Lagrange point, and the Helioseismic and Magnetic Imager (HMI) (HMI, 2010) onboard the Solar Dynamics Observatory (SDO) (Pesnell, D. and Patel A., 2020; Pesnell et al., 2012), orbiting the Earth on a heliosynchronous orbit.

The SDO represents the newest of these three sources and offers data of the highest quality and resolution. A comparison between the resolutions of SOHO's MDI and SDO's HMI is illustrated in Fig. 2.2. Additionally, a relatively recent project, the Polarimetric and Helioseismic Imager (PHI), launched in 2020, aims to provide data in the same Fraunhofer emission line as the HMI (Solanki et al., 2020).

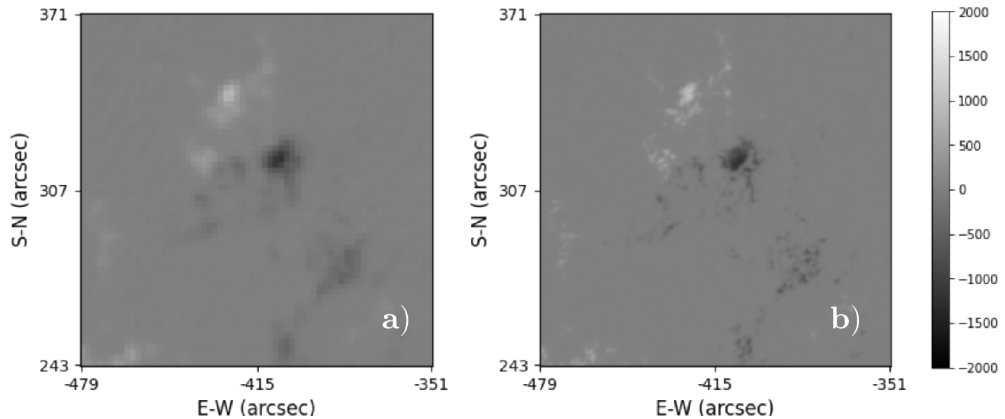


Figure 2.2: Comparison of line-of-sight magnetograms taken by SOHO/MDI (left) and SDO/HMI (right). Both images were captured at 00:00:00 UT on 1 May 2010. Credit: Xu et al. (2024).

In the context of global helioseismology, it's generally not feasible to neglect the curvature of the Sun when examining the entire solar sphere. Therefore, the signal is decomposed into spherical harmonics. In local helioseismology, the typical procedure involves selecting a small region of the Sun and tracking it within a co-rotation frame. This process yields a sequence of Dopplergrams, each representing a snapshot of this area at different times. Subsequently, the Postel azimuthal equidistant projection (refer to Sec. 5.3) is commonly applied, followed by the Fourier transform.

The signal $\Phi(\mathbf{r}, t)$, typically presented as a sequence of line-of-sight velocity Dopplergrams, where $\mathbf{r} = (x, y)$, undergoes transformation to plane-parallel geometry through the Fourier transform:

$$\Phi(\mathbf{k}, \omega) = \int_A d^2\mathbf{r} \int_0^T dt \Phi(\mathbf{r}, t) e^{-i(\mathbf{k}\cdot\mathbf{r} - \omega t)}, \quad (2.19)$$

where A represents the area of the observed surface, and T signifies the total observation time. Here, $\mathbf{k} = (k_x, k_y)$ denotes the horizontal wave vector, while ω stands for the angular frequency. The standard convention dictates that the x coordinate is positive in the direction of solar rotation, and positive y points north.

The power spectrum $P(\mathbf{k}, \omega)$ is defined as

$$P(\mathbf{k}, \omega) = |\Phi(\mathbf{k}, \omega)|^2. \quad (2.20)$$

It clearly shows us the presence of oscillations which manifest themselves as resonances in the power spectrum as shown in Fig. 2.3.

The power spectrum contains information about various oscillation modes. To distinguish between them, special filters are applied to the data. The two most commonly used types of filters are *ridge filters* and *phase speed filters*. Ridge filters, referred to as f and p1 – p4 hereafter, selectively isolate waves of a specific mode, such as the f mode. These waves penetrate to different depths in the Sun, scanning various internal regions, but their signal is stronger due to resonances. Phase speed filters, referred to as td1 – td11 hereafter, select waves with a given phase velocity, indicating waves that penetrate to the same depths. All filters, both ridge and phase speed, applicable to a power spectrum, are depicted in Fig. 2.4. A table with parameters of phase speed filters can be found in (e.g. Gizon and Birch, 2005; Couvidat and Birch, 2006).

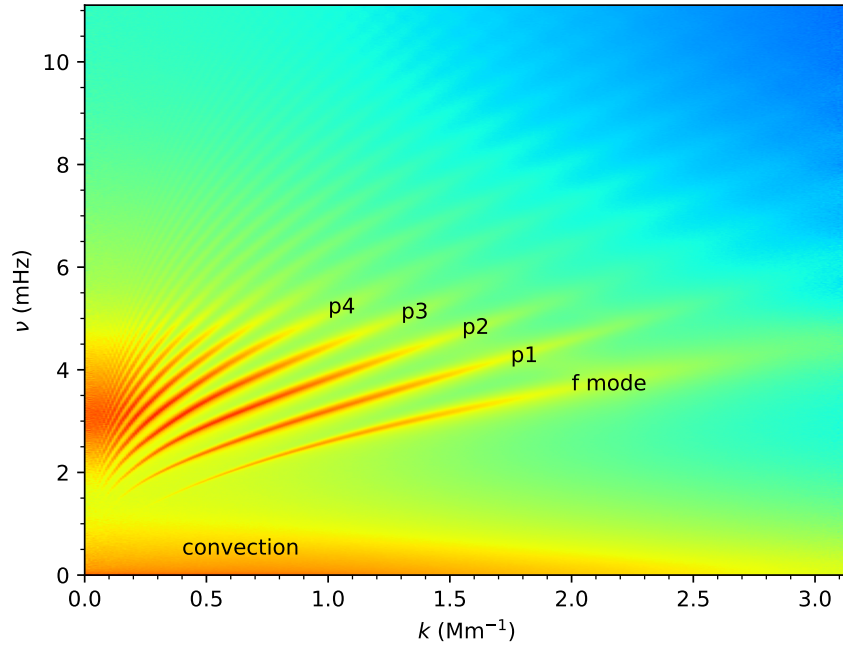


Figure 2.3: A power spectrum created from observations from SDO/HMI. The surface gravity wave (f mode) and sound waves (p modes) are labeled in the plot together with the resonance signal created by convection. The strong resonance present at $\nu \approx 3$ mHz for low k is the five-minute oscillation discovered by Leighton (1963).

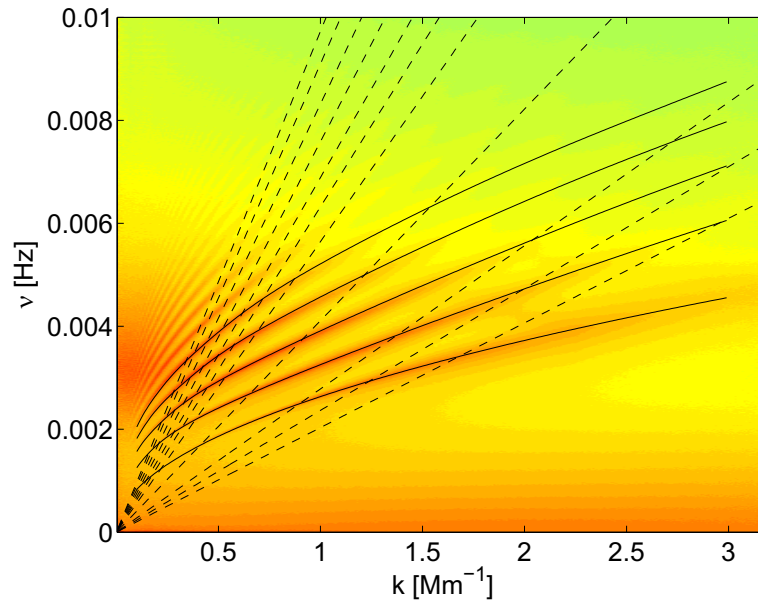


Figure 2.4: A power spectrum with shown ridge filters (full line) and phase speed filters (dashed line).

3. Helioseismology

Helioseismology encompasses a set of methods enabling us to examine the inner composition and dynamics of the Sun through the analysis of solar oscillations. Although not widely known to the public, it stands as one of the most successful fields of astrophysics, as described by Buldgen (2019). Buldgen (2019) further exemplifies this success by citing instances such as the determination of solar photospheric helium abundance, typically inaccessible due to spectroscopic constraints, the localization of the base of the convective zone, and the demonstration of the significance of microscopic diffusion in stellar radiative regions. Moreover, since the dispersion relation of different types of waves depends on the conditions along their trajectory, helioseismology allows us to determine subsurface structures and conditions.

Modern helioseismology is divided into two main subfields: global and local helioseismology. Global helioseismology focuses on studying large-scale features of the Sun, such as the rotational profile. As this aspect is not the primary focus of this work, we won't delve into it further, but we encourage readers to explore Buldgen (2019); Christensen-Dalsgaard (2002); Korda (2020) for more detailed insights on this topic.

3.1 Local helioseismology

The second field of helioseismology concentrates solely on a specific region of the Sun's surface. The wave field within the chosen region is influenced by the properties of that particular area, both on the surface and beneath it. Consequently, by analyzing the wave patterns in this local region, it becomes possible to deduce local 3-D structures and dynamics beneath the surface (Christensen-Dalsgaard, 2002). However, the emphasis on a relatively small area of the solar disk requires a much higher signal-to-noise ratio compared to global helioseismology, thus underscoring the importance of high-precision measurements.

As mentioned in the sections about solar oscillations observations, Sec. 2.3, the standard procedure used in all methods of local helioseismology involves selecting a small region on the Sun's surface and tracking it within a co-rotation frame, i.e. the region does not move in time relative to the surface of the Sun. From the practical point of view, this approach means that we select only some portion of the data, based on the selected region, from each Dopplergram in a sequence.

One of the common methods in local helioseismology is the *ring-diagram* analysis. In this method, a cut at a constant frequency ω is extracted from a 3-D power spectrum $P(k_x, k_y, \omega)$, i.e., $P(k_x, k_y, \omega = \text{const.})$. The ridges in the original power spectrum appear as concentric circles with a center at $(k_x = 0, k_y = 0)$. The ring with the largest radius corresponds to the lowest-order observable mode for the given frequency. If there are any local sound speed perturbations present in the area, they will manifest themselves by altering the radius of the circles. Conversely, any flows will distort the circles, causing them to become non-concentric or elliptical. An example of a ring diagram is illustrated in Fig. 3.1.

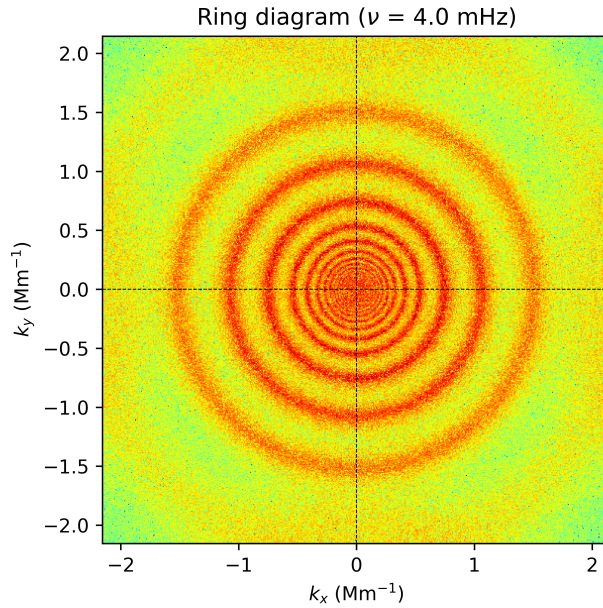


Figure 3.1: A ring diagram created from a power spectrum of a 24 h observation by SDO/HMI at a constant frequency $\nu = 4$ mHz.

Another commonly used method is called *time-distance helioseismology* and is discussed in the following section.

3.2 Time-distance helioseismology

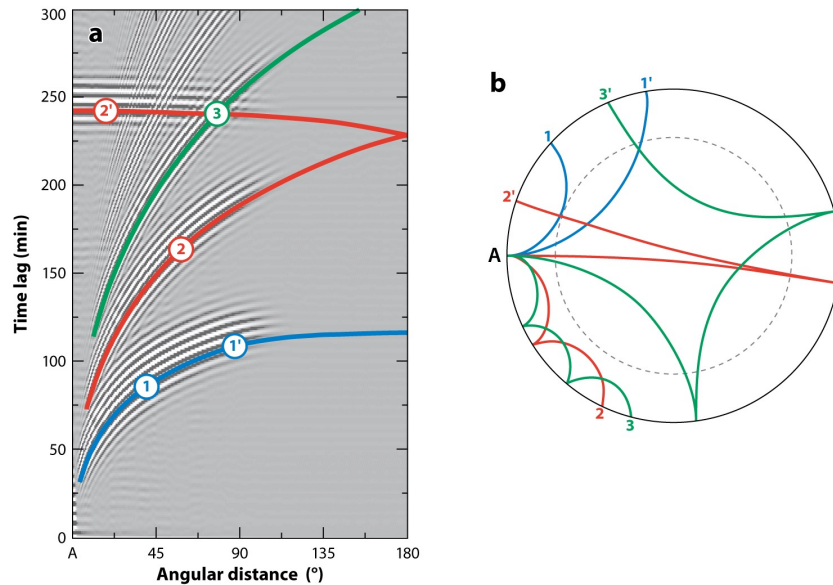
The time-distance helioseismology described by Gizon and Birch (2005); Gizon et al. (2010); Kosovichev (2011); Christensen-Dalsgaard (2002) aims to provide information about the solar interior based measuring the travel-time τ of acoustic (p modes) and surface gravity (f modes) waves propagating from point \mathbf{r}_1 to a different point \mathbf{r}_2 . The travel time is dependent on the conditions along the wave trajectory such as density, sound speed and material flows.

Initially, the vigorous convection induces a minor perturbation in the background stable conditions at point \mathbf{r}_1 , which propagates as a wave, similarly to the trajectory of light in geometrical optics. The increase in sound speed towards the solar center causes the wave packet to deviate away from a normal line. Waves with frequencies $\omega < \omega_c$ are bound by lower and upper turning points r_{low} and r_{up} as described in more detail in Sec. 2.2. Waves of higher frequencies escape into the solar atmosphere.

A schematic representation of the time-distance method is shown in Fig. 3.2. It illustrates sources of perturbations on the solar surface and the propagation of waves through the solar interior, culminating in detection at the surface. Some waves pass through anomalies, such as sound-speed perturbations or vector flows. By comparing waves propagating through these anomalies with those that do not, we can localize and quantify the given anomaly and its cause.

Due to the greater spatial resolution of the method (compared to the ring-diagram method mentioned earlier), the data are filled with more realization noise. The primary source of noise is subsurface convection, which generates a plethora of waves. To improve the signal-to-noise ratio, the signal undergoes temporal averaging. Initially, the observed area is tracked with local angular velocity, and the curvature of the Sun is typically neglected in local helioseismology. Subsequently, the data, often Dopplergrams (see Sec. 5.2), are remapped using the Postel azimuthal equidistant projection (see Sec. 5.3) and filtered. In the Fourier domain, a filter $F(\mathbf{k}, \omega)$ selects waves with desired properties, typically targeting supergranulation and granulation noises for removal. Due to distinct dispersion relations of f and p modes, the signal of each wave type is processed separately.

For p modes, both ridge and phase-speed filters are employed. Ridge filters utilize eigenvalues of the reference model, with filter width chosen to avoid signal from neighboring ridges. Phase-speed filters eliminate waves with identical phase speeds, with deeper penetration corresponding to higher phase speeds. In contrast, for f modes, only ridge filters are applied. The resulting filtered data $\Psi(\mathbf{k}, \omega) = F(\mathbf{k}, \omega)\Phi(\mathbf{k}, \omega)$, with the composite filter (removing granulation + either ridge filter or phase speed filter) being applied on the signal $\Phi(\mathbf{k}, \omega)$, serve as input for subsequent processing.




 Gizon L, et al. 2010.
Annu. Rev. Astron. Astrophys. 48:289–338

Figure 3.2: (a) Measured cross-covariance function for SDO/MDI medium-degree data as a function of separation distance and time lag. Positive values are white; negative values are black. The observation duration is $T = 144$ days starting in May 1996. (b) Example ray paths for acoustic wavepackets. In both a and b, the blue lines correspond to single-skip ray paths, the red lines are for two-skip ray paths, and the green lines are for three-skip ray paths. Credit: Gizon et al. (2010).

A standard method for determining travel times within the noise-filled signal $\Psi(\mathbf{k}, \omega)$ involves identifying similarities within the data, i.e. calculating the temporal cross-covariance of the signal between two points in space and time (Gizon and Birch, 2005):

$$C(\mathbf{r}_1, \mathbf{r}_2, t) = \frac{h_t}{T - |t|} \sum_{t'} \Psi(\mathbf{r}_1, t') \Psi(\mathbf{r}_2, t' + t) \approx \int_0^T \Psi(\mathbf{r}_1, t') \Psi(\mathbf{r}_2, t' + t) dt', \quad (3.1)$$

where h_t is the temporal sampling and T is the duration of observation. A visual representation of the cross-covariance function is the time-distance diagram shown in Fig. 3.2. The positive time lags are obtained from waves travelling from the point \mathbf{r}_1 to \mathbf{r}_2 while the negative time lag arises from waves moving in the opposite direction.

3.2.1 Travel times

In realistic applications, the cross-covariance function measured for two points contains a large amount of realization noise due to the stochastic nature of solar oscillations. Hence, it is almost impossible to measure the travel time of the waves traveling between two individual pixels in the helioseismic observables. Usually, some averaging is required. Most often, such averaging is applied both in time and space. In time, cross-covariances are usually averaged over a time period T larger than about 6 hours, with most results using averages over 8 or 24 hours. To further improve the signal-to-noise ratio, it was first suggested by Duvall et al. (1993) to average cross-covariance $C(\mathbf{r}_1, \mathbf{r}_2, t)$ over points \mathbf{r}_2 that belong to the annulus or quadrants centered at \mathbf{r}_1 with a distance $\Delta = |\mathbf{r}_2 - \mathbf{r}_1|$. For the study of the waves traveling from the central point towards the surrounding annulus and in the opposite direction, averaging over a full annulus is suitable. For the investigation of the waves traveling in the direction parallel to the equator (east–west), averaging over 90-degree quadrants of the annulus in the corresponding direction is more suitable. In the methodology used in this study, quadrants were replaced by sections of the annulus multiplied by the cosine (east–west direction) or sine (south–north direction) of the horizontal polar angle. These geometries constitute a smooth continuous transition from quadrant geometries.

For a given set of \mathbf{r}_1 and Δ , the cross-covariance function oscillates around a characteristic travel time in both the positive and negative part of the time axis. The fitting of the travel time is often performed by fitting the Gaussian wavelet, enabling the evaluation of both the phase and group travel times, allowing for the development of a phase of the wavelet during the wave propagation. In reality, one fits the function

$$C_+(t; \mathbf{r}_1, \Delta) = A \exp[-\gamma^2(t - t_g)^2] \cos[\omega_0(t - \tau_+)], \quad (3.2)$$

where t_g represents the group travel time and τ_+ the positive phase travel time. Parameters A and γ describe the amplitude and decay rate of the wavelet envelope.

An analogous equation may be written for a negative travel time. The time–distance analysis relies on measurement and interpretation of the phase travel times τ_+ and τ_- .

The fitting of the Gaussian wavelet is demanding and often fails due to the presence of noise. Therefore, alternative definitions of travel times were developed that are more robust in the presence of noise. They stem from the fact that the cross-covariance of the waves may be computed from the solar model by solving the equations of the wave propagation. These cross-covariances represent some sort of a reference for a spherically symmetrical 1-D quiet Sun. We may safely assume that the changes to the cross-covariances caused by the perturbations of the model will introduce a modification of the background-model cross-covariances. Then, instead of fitting a 5-parameter Gaussian wavelet, we may use this reference cross-covariance as a template and perform only 1-parameter fitting in time. Such an approach is used also in geoseismology (Zhao and Jordan, 1998) and for the need of the time–distance helioseismology was devised by Gizon and Birch (2002). Following the paper we refer to, these travel times are termed GB02 travel times henceforth.

Later, Gizon and Birch (2004) simplified this definition even further for the case of very small perturbations. Such a robust definition allows the measurement of travel times averaged over a short time (e.g., around $T = 2$ hours) and with a large spatial resolution. According to the so-called GB04 definition, the travel time may be computed as

$$\tau_{\pm}(\mathbf{r}_1, \mathbf{r}_2) = h_t \sum_t W_{\pm}(\Delta, t) [C(\mathbf{r}_1, \mathbf{r}_2, t) - C^0(\Delta, t)], \quad (3.3)$$

where h_t is a sampling in time, C^0 represents the reference cross-covariance, and the weighting functions W_{\pm} are defined by

$$W_{\pm}(\Delta, t) = \frac{\mp f(\pm t) \partial_t C^0(\Delta, t)}{h_t \sum_{t'} f(\pm t') [\partial_{t'} C^0(\Delta, t')]^2}. \quad (3.4)$$

Here the window functions $f(\pm t)$ are used to separate positive and negative travel times (waves travelling in an opposite direction) and are usually chosen as band-pass filters keeping only cross-covariances around the first-skip arrival times of the waves that would correspond to the values around $\pm t_g$ from (3.2).

We note that both GB02 and GB04 definitions of the travel times result in a travel time that is a mixture of both the group and phase travel times. It is not straightforward to decouple the two. A proper choice of the reference cross-covariance C^0 is essential to minimize the contribution of the group travel time to the results. In some cases, a reference cross-covariance coming from the forward modeling does not have to be accurate enough. In those cases, a construction of the reference cross-covariance as a spatial average of different realizations over the field of view in the quiet-Sun regions may be a better choice.

3.2.2 Travel-time sensitivity kernels

The travel times are quantities measured from the properties of helioseismic observables, such as Doppler shifts or intensities. As already discussed in previous chapters, these travel times can be computed from the solar model using forward modeling. Additionally, we mentioned that changes in the models with respect to the reference lead to changes in the travel times.

It is straightforward, therefore, to switch from travel times τ to travel-time deviations $\delta\tau$ with respect to the unperturbed travel time τ_0 :

$$\delta\tau(\mathbf{r}) = \tau(\mathbf{r}) - \tau_0(\mathbf{r}). \quad (3.5)$$

Let us consider that the solar model is fully described by a multidimensional vector of quantities $Q^\alpha(\mathbf{x})$, where the index α lists the considered physical quantities. These quantities may, for instance, be vector flows \mathbf{v} , sound speed c , density ρ , adiabatic exponent Γ , among others. The quantities Q^α are functions of 3D spatial coordinates and, in principle, also of time. However, we will only consider stationary models in terms of the averaging over the observation interval T .

Similarly to the discussion of the travel times, we may split the values of the quantities into the unperturbed background $Q_0^\alpha(\mathbf{x})$, which in most cases is represented by the background solar model, and the perturbation $q^\alpha(\mathbf{x})$.

To compute the linear adiabatic oscillations of the Sun, methodologies have been available for a very long time (Lynden-Bell and Ostriker, 1967). Such a computation is slow and expensive even when considering the computational power of today's computers. This approach is not viable when dealing with realistic problems.

If we focus only on linear perturbations of the model, we may relate travel-time deviations $\delta\tau$ with perturbations of the solar model q^α by an equation.

$$\delta\tau^a(\mathbf{r}) = \sum_\alpha \int_{\odot} d^2\mathbf{r}' dz \mathbf{K}_\alpha^a(\mathbf{r}' - \mathbf{r}, z) \cdot q^\alpha(\mathbf{r}', z) + n^a(\mathbf{r}). \quad (3.6)$$

The index a represents the so-called travel-time geometry and combines the choice of the $k - \omega$ filter (see 2.3), point-to-annulus or point-to-quadrant averaging, and the radius of the annulus Δ . Measured travel times are subject to random realization noise n^a . The quantity \mathbf{K}_α^a is termed a *sensitivity kernel* and represents a function that "translates" changes in the solar model into travel-time deviations.

The assumption of small perturbations allows us to split the total travel-time deviation into individual contributions by individual perturbers α . For example, when considering model changes due to sound-speed perturbations $\frac{\delta c^2}{c_0^2}$, density changes $\frac{\delta \rho}{\rho_0}$, pressure deviations $\frac{\delta P}{P_0}$, and flows \mathbf{v} , equation (3.6) becomes:

$$\delta\tau^a(\mathbf{r}) = \int_{\odot} d^2\mathbf{r}' dz \left[K^{c^2}(\mathbf{r}' - \mathbf{r}, z) \frac{\delta c^2}{c_0^2}(\mathbf{r}', z) + K^\rho(\mathbf{r}' - \mathbf{r}, z) \frac{\delta \rho}{\rho_0}(\mathbf{r}', z) + K^P(\mathbf{r}' - \mathbf{r}, z) \frac{\delta P}{P_0}(\mathbf{r}', z) + \sum_{i=1}^3 K^{v_i}(\mathbf{r}' - \mathbf{r}, z) v_i(\mathbf{r}', z) \right] + n^a(\mathbf{r}). \quad (3.7)$$

In our study, we primarily focused on the flows \mathbf{v} . It is important to note that sensitivity kernels can similarly be derived and used for observable quantities other than travel times. In the literature, we find kernels for frequency deviations and even for cross-covariances. The latter case is referred to as *full-waveform* sensitivity kernels.

Sensitivity kernel functions are calculated numerically using the background solar model. Various approaches have been developed by different authors. The simplest approximation ignores the finite-wavelength effects and assumes the propagation of waves along their optimal rays. This ray approximation employs the principles of geometrical optics (see Kosovichev and Duvall, 1997, and references therein).

Finite-wavelength effects are considered by approximating wave propagation in terms of scattering. Single-source sensitivity kernels were proposed and computed, for example, by (Birch and Kosovichev, 2000). This approach was motivated by similar methods used in geoseismology.

Unlike on Earth, there is never a single source of waves on the Sun. The waves are excited by processes in granules that are randomly distributed across the entire solar surface. Consequently, sensitivity kernels considering randomly distributed sources were proposed and developed by (Gizon and Birch, 2002). Later, a linearized approach consistent with the definition of linearized travel times was proposed by (Gizon and Birch, 2004). Gizon & Birch emphasized the importance of incorporating data processing steps—not only the $k - \omega$ filtering but also an accurate estimate of the telescope’s point spread function—into the calculation of the kernels, ensuring they align with the measured travel times. For details of the kernel calculation, we refer to (Burston et al., 2015).

4. Methodology

The aim of this thesis is to test the validity of velocity (flow) perturbation sensitivity kernel integrals, numerically computed using the background solar model (see Sec. 3.2.2 and literature therein), with a model-independent method. This section provides an explanation of the method used and the methodology of its execution. It is important to note that our method verifies only the validity of the volume integral of the velocity (flow) sensitivity kernel. It does not provide validation for volume integrals of other sensitivity kernels or the kernels themselves.

The first step of the method is to inject an artificial constant longitudinal flow (velocity perturbation) \mathbf{v}_0 into data from observations. This is achieved by moving the selected region on the solar disk (see Sec. 3.1) relative to the surface with a velocity equal to the injected constant velocity. Consequently, while in all standard procedures of local helioseismology the region follows the Carrington rotation to track the same area over time, in our case, the region moves faster or slower than the Carrington rotation, depending on the sign of the injected velocity.

This effectively means that to all perturbations q^α mentioned in Eq. 3.6, an additional perturbation \mathbf{v}_0 representing the constant injected velocity is added, transforming the equation into

$$\delta\tau^a(\mathbf{r}) = \sum_\alpha \int_{\odot} d^2\mathbf{r}' dz \mathbf{K}_\alpha^a(\mathbf{r}' - \mathbf{r}, z) \cdot [q^\alpha(\mathbf{r}', z) - \mathbf{v}_0] + n^a(\mathbf{r}) . \quad (4.1)$$

The reason there is a minus sign in the term $[q^\alpha(\mathbf{r}', z) - \mathbf{v}_0]$ is that we inject the artificial flow by moving the coordinate frame. However, moving the frame in one direction corresponds to an apparent flow of the same velocity but in the opposite direction, similarly to watching a landscape passing by through the window of a moving train. Eq. 4.1 can be rewritten as

$$\begin{aligned} \delta\tau^a(\mathbf{r}) = & \sum_\alpha \int_{\odot} d^2\mathbf{r}' dz \mathbf{K}_\alpha^a(\mathbf{r}' - \mathbf{r}, z) \cdot q^\alpha(\mathbf{r}', z) \\ & - \int_{\odot} d^2\mathbf{r}' dz \mathbf{K}_v^a(\mathbf{r}' - \mathbf{r}, z) \cdot \mathbf{v}_0 + n^a(\mathbf{r}) , \end{aligned} \quad (4.2)$$

where \mathbf{K}_v^a is the sensitivity kernel for a velocity (flow) perturbation. Since the injected velocity is constant, i.e., each pixel of the frame moves with the same velocity, the corresponding flow \mathbf{v}_0 is independent of position. Therefore, it is not affected by the volume integral and can be taken out of it:

$$\begin{aligned} \delta\tau^a(\mathbf{r}) = & \sum_\alpha \int_{\odot} d^2\mathbf{r}' dz \mathbf{K}_\alpha^a(\mathbf{r}' - \mathbf{r}, z) \cdot q^\alpha(\mathbf{r}', z) \\ & - \mathbf{v}_0 \int_{\odot} d^2\mathbf{r}' dz \mathbf{K}_v^a(\mathbf{r}' - \mathbf{r}, z) + n^a(\mathbf{r}) . \end{aligned} \quad (4.3)$$

Further, an averaging over a central area is applied, transforming the Eq. 4.3 into the form

$$\begin{aligned} \langle \delta\tau^a(\mathbf{r}) \rangle = & \left\langle \sum_{\alpha} \int_{\odot} d^2\mathbf{r}' dz \mathbf{K}_{\alpha}^a(\mathbf{r}' - \mathbf{r}, z) \cdot q^{\alpha}(\mathbf{r}', z) \right\rangle \\ & - \left\langle v_0 \int_{\odot} d^2\mathbf{r}' dz \mathbf{K}_v^a(\mathbf{r}' - \mathbf{r}, z) \right\rangle + \langle n^a(\mathbf{r}) \rangle . \end{aligned} \quad (4.4)$$

The first term on the right side of Eq. 4.4 can be viewed as a certain average background travel time perturbation which is unaffected by the implanted velocity. The second term is independent of position, therefore the averaging won't affect it and it remains unchanged from before the averaging. The contribution of the realization noise is negligible after the averaging due to its random nature. Therefore, Eq. 4.4 can be written as

$$\langle \delta\tau^a(\mathbf{r}) \rangle = \langle \delta\tau_{\text{back}}^a(\mathbf{r}) \rangle - v_0 \int_{\odot} d^2\mathbf{r}' dz \mathbf{K}_v^a(\mathbf{r}' - \mathbf{r}, z). \quad (4.5)$$

As one can conclude from Eq. 4.5, an average travel time perturbation in a selected central area of the tracked region is directly proportional to the volume integral of the velocity perturbation kernel with the injected velocity acting as a constant of proportionality. Therefore, for each observation (sequence of Dopplergrams, see Sec. 5.2) in one configuration (wave filter, annulus radius - see Sec. 5.5), we get a mean travel time perturbation as a linear function of the injected velocity, with the volume integral of the velocity perturbation kernel acting as a slope and the background perturbation as a vertical shift.

By repeating this process for various injected velocities, the set of average travel time perturbations can be plotted against the set of injected velocities. The volume integral of the velocity perturbation kernel can then be determined from a linear fit. The injected velocity is a pre-determined constant value and the average travel time perturbation is calculated from the observational data, in other words, both quantities are model-independent, therefore the obtained value of the volume integral is also model-independent.

By doing the same process for all wave filters (ridge filters f and p1 - p4, phase speed filters td1 - td11) and various annulus radii, we obtain a set of model-independent volume integrals of velocity perturbation kernels. We can then compare them to integrals calculated from a model(s). That is done by plotting the model-independent integrals against the model ones and fitting the dependency.

5. Data analysis

This chapter aims to present the sources of data analyzed in this thesis and their types, together with the commonly used projection technique (Sec. 5.2 – 5.3). Furthermore, two data analysis pipelines that form the core of this work are presented and explained in detail (Sec. 5.4 – 5.5).

5.1 Source of Data - SDO/HMI

All the data used and analyzed in this thesis were measured by NASA’s Solar Dynamics Observatory (SDO) launched on 11 February 2010. SDO provides the following observations (quoted from Pesnell, D. and Patel A. (2020)):

1. Measure the extreme ultraviolet spectral irradiance of the Sun at a rapid cadence
2. Measure the Doppler shifts due to oscillation velocities over the entire visible disk
3. Make high-resolution measurements of the longitudinal and vector magnetic field over the entire visible disk
4. Make images of the chromosphere and inner corona at several temperatures at a rapid cadence
5. Make those measurements over a significant portion of a solar cycle to capture the solar variations that may exist in different time periods of a solar cycle

These observations are provided by SDO’s three main instruments shown on the SDO spacecraft in Fig. 5.1 (Pesnell et al., 2012):

1. Helioseismic and Magnetic Imager (HMI): Measures solar magnetic fields and provides data on the Sun’s interior structure and dynamics, aiding in the study of solar variability and its effects on space weather.
2. Atmospheric Imaging Assembly (AIA): Captures high-resolution images of the solar atmosphere across multiple wavelengths, providing insights into various layers and phenomena such as flares and coronal loops.
3. Extreme Ultraviolet Variability Experiment (EVE): Monitors the Sun’s extreme ultraviolet (EUV) radiation, crucial for understanding solar variability and its impact on Earth’s atmosphere and climate.

This suite of instruments observes the Sun continuously, generating approximately a terabyte of data each day. The instrument of particular interest for this thesis is HMI, which studies oscillations and magnetic fields at the solar surface. It covers the full solar disk at the 6173 Å Fraunhofer line with a resolution of 1 arcsec. HMI is a successor to the Michelson Doppler Imager on the Solar and Heliospheric Observatory (SOHO) and provides both Doppler images of the Sun (Dopplergrams) as well as magnetograms (Pesnell et al., 2012; Pesnell, D. and Patel A., 2020; HMI, 2010).

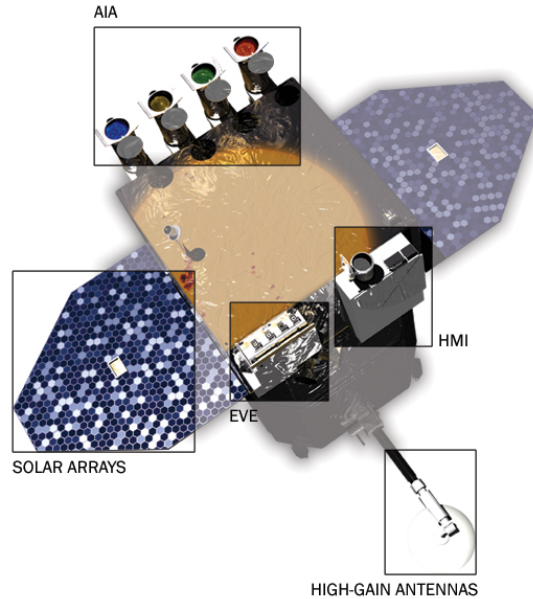


Figure 5.1: An image of SDO spacecraft with the main instruments HMI, AIA and EVE highlighted. Credit: NASA SDO (sdo.gsfc.nasa.gov).

5.2 HMI Dopplergrams

A Dopplergram constitutes a representation of line-of-sight solar surface velocities derived from Doppler shift measurements of a Fraunhofer absorption line. An exemplary Dopplergram is depicted in Fig. 5.2. The Sun’s rotation is discernible through the obvious brightness contrast between its left and right disc regions. Additionally, a distinct “cellular pattern,” stemming from supergranulation, is evident within the image. HMI generates comprehensive Dopplergram series throughout the day, with cadences of 45 seconds. Each Dopplergram is captured with a resolution of 4096×4096 . The entirety of HMI and AIA data, including Dopplergrams, is archived and managed by the Joint Science Operations Center (JSOC).

HMI scans the Fe^I 617.3 nm photospheric absorption line and measures the intensity across different polarization states. In the standard regime, a sequence of filtergrams is obtained by scanning the spectral line at six wavelength positions, each 7.6 pm apart, across various polarimetric states. The raw, unprocessed filtergrams in polarized light constitute the level 0 series, which is available only upon request. After undergoing flat-fielding and other calibration procedures, primary filtergrams are stored as level 1 data, accessible from the JSOC. From the level 1 data, various data products are computed, including Dopplergrams.

These Dopplergrams are stored within the series `hmi.V_45s` at JSOC and are computed using a fast "MDI-like algorithm". This algorithm employs the Fourier coefficients that describe the spectral-line shape $I(\lambda)$ by a limited number of values, specifically:

$$a_1 = \frac{2}{T} \int_{-\frac{T}{2}}^{+\frac{T}{2}} I(\lambda) \cos\left(2\pi \frac{\lambda}{T}\right), \quad (5.1)$$

$$b_1 = \frac{2}{T} \int_{-\frac{T}{2}}^{+\frac{T}{2}} I(\lambda) \sin\left(2\pi \frac{\lambda}{T}\right), \quad (5.2)$$

$$a_2 = \frac{2}{T} \int_{-\frac{T}{2}}^{+\frac{T}{2}} I(\lambda) \cos\left(4\pi \frac{\lambda}{T}\right), \quad (5.3)$$

$$b_2 = \frac{2}{T} \int_{-\frac{T}{2}}^{+\frac{T}{2}} I(\lambda) \sin\left(4\pi \frac{\lambda}{T}\right). \quad (5.4)$$

where T is the "period" of the line profile, empirically taken to be 6 times the wavelength separation between 2 filters (hence $T = 41.28$ nm). When assuming that the spectral line has a Gaussian profile

$$I(\lambda) = I_c - I_d \exp\left[-\frac{(\lambda - \lambda_0)^2}{\sigma^2}\right], \quad (5.5)$$

where I_c is the intensity of the neighbouring continuum, I_d is the line depth, λ_0 the nominal position of the line and σ is the line width, then the Doppler velocity corresponding to the line shift may be computed as

$$v_{\text{los}} = \frac{dv}{d\lambda} \frac{T}{2\pi} \text{atan}\left(\frac{b_1}{a_1}\right) \quad (5.6)$$

or from the second Fourier coefficients

$$v_{\text{los}} = \frac{dv}{d\lambda} \frac{T}{4\pi} \text{atan}\left(\frac{b_2}{a_2}\right). \quad (5.7)$$

The fraction $\frac{dv}{d\lambda} = 299792458.0/6173.3433 = 48562.4 \text{ ms}^{-1}/\text{\AA}$ is derived from the standard Doppler-shift formula.

HMI instrument samples the iron line at only six points, the proper description of the spectral line profile is not known. When assuming that the HMI transmission profiles at the six positions are delta functions, the Fourier coefficients may be approximated as

$$a_1 \approx \frac{2}{6} \sum_{i=0}^5 I_j \cos \left(2\pi \frac{2.5 - j}{6} \right), \quad (5.8)$$

$$b_1 \approx \frac{2}{6} \sum_{i=0}^5 I_j \sin \left(2\pi \frac{2.5 - j}{6} \right), \quad (5.9)$$

$$a_2 \approx \frac{2}{6} \sum_{i=0}^5 I_j \cos \left(4\pi \frac{2.5 - j}{6} \right), \quad (5.10)$$

$$b_1 \approx \frac{2}{6} \sum_{i=0}^5 I_j \sin \left(4\pi \frac{2.5 - j}{6} \right), \quad (5.11)$$

$$(5.12)$$

where I_j represents the intensity measured at the j -th spectral-line position.

Practically, the MDI-like algorithm utilizes the discrete approximation of the first Fourier coefficients a_1 and a_2 of the Fe^I line to estimate the line-of-sight velocity using formula (5.6). However, since the transmission profiles are not delta functions, the Doppler velocity estimate is corrected using a set of correction coefficients. This adjustment is conducted at the data center using a lookup table, which was precomputed to numerically estimate the effects of certain assumptions being violated (finite width of the transmission profiles, non-Gaussian spectral-line profile, sparse sampling of the spectral line).

Filter transmission profiles are regularly measured and exhibit slow changes over time. Consequently, another correction is applied to account for long-term variations in the derived values. The Doppler velocities are computed separately for filter positions taken in the left circular polarized light and right circular polarized light and are averaged at the final stage. The results are then stored in the data series.

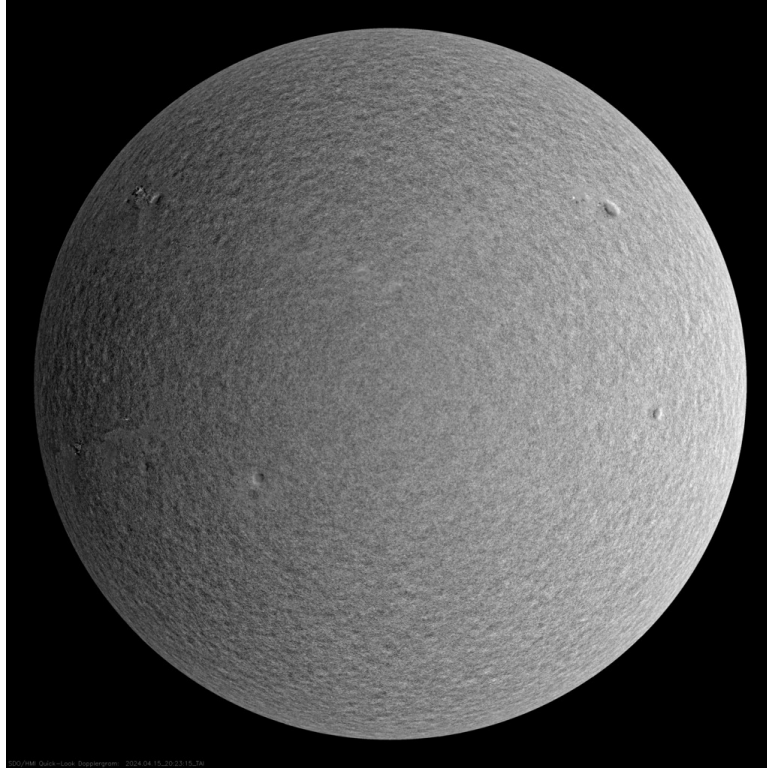


Figure 5.2: A Dopplergram from 04/15/2024 acquired by SDO/HMI. Credit: NASA SDO (sdo.gsfc.nasa.gov).

5.3 Azimuthal equidistant (Postel) projection

The azimuthal equidistant projection is classified as a map projection that preserves both distance and direction from the central point of projection to any other point on the map. The projection is equidistant, meaning all distances measured from the central point to all other points on the map are accurately represented. This makes it valuable for applications requiring accurate distance measurements from a specific location such as navigational charts, meteorological maps, and astronomical charts. Postel projection also preserves main circles on the sphere, hence it is appropriate for the time–distance analysis with the point-to-annulus and point-to-quadrant averaging geometries.

While the azimuthal equidistant projection excels in preserving distances from the central point, it inevitably introduces distortion in other map properties. Notably, this projection sacrifices accuracy in shape, area, and scale, especially as one moves away from the central point of projection (Snyder and Voxland, 1989) as shown in Fig. 5.3. As a result, the further away from the central point, the greater the distortion becomes. However, within the vicinity of the central point, the azimuthal equidistant projection offers an accurate representation of distances and directions, making it invaluable for localized mapping and analysis (Snyder, 1997).

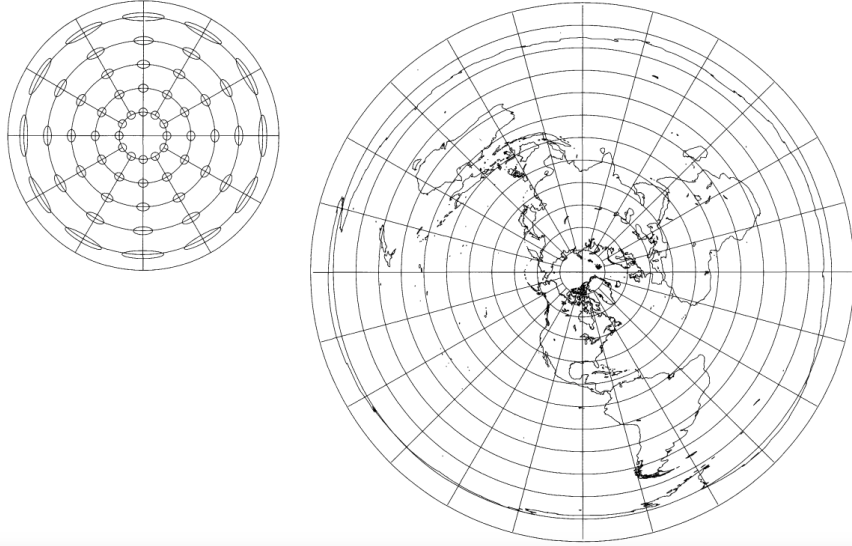


Figure 5.3: Azimuthal equidistant (Postel) projection centered in Earth's north pole (right) and a distortion map of the projection (left). Credit: Snyder and Voxland (1989).

The rectangular coordinates for the azimuthal equidistant projection for a given sphere radius R , latitude ϕ and longitude λ are (Snyder and Voxland, 1989; Neacsu M., 2024):

$$x = Rk' \cos \phi \sin (\lambda - \lambda_0) \ , \quad (5.13)$$

$$y = Rk' [\cos \phi_0 \sin \phi - \sin \phi_0 \cos \phi \cos (\lambda - \lambda_0)] \ , \quad (5.14)$$

where ϕ_0 and λ_0 are latitude and longitude of the center of projection, c is the angular distance from the center and c and k' follow (Snyder and Voxland, 1989; Neacsu M., 2024):

$$k' = \frac{c}{\sin c} \ , \quad (5.15)$$

$$\cos c = \sin \phi_0 \sin \phi + \cos \phi_0 \cos \phi \cos (\lambda - \lambda_0) \ . \quad (5.16)$$

5.4 Tracking pipeline

The tracking pipeline is responsible for preparing datacubes passed into the travel-time pipeline described in Sec. 5.5. In addition to traditional steps such as selecting the local area, applying the azimuthal equidistant projection, and creating the datacube in FITS format with a correct header, this pipeline offers an additional feature specific to this work: implanting artificial velocities by moving the selected area at a predefined speed. This is a crucial feature used in determining the model-independent velocity kernels as explained in Chap. 4, Methodology.

Since this is not part of standard pipelines for datacube preparation, our own solution was necessary.

At a high level, the tracking pipeline performs the following:

1. Prepare the folder structure together with all necessary configuration files (both for the datacube creation step and for the subsequent travel-time pipeline) based on the input configuration (JSOC DRMS queries, data PATHs, projection origins, implanted velocities).
2. (OPTIONAL) Download data (Dopplergrams) from JSOC. This step is unnecessary when the required data are already downloaded.
3. Create a datacube for each combination of DRMS query and velocity and save it in the form of a FITS file into its designated folder prepared in step 1.

These three steps are implemented as three separate pipelines (scripts) so the user has the ability to check the outcome of each step before proceeding, which is essential for steps 1 and 2 as their successful execution is vital for a correct run of the datacube pipeline in step 3. Moreover, the pipelines in steps 2 and 3 are optimized both for running on a local machine and on a cluster with a PBS/Torque job management system (for our use-case, a small cluster in Ondřejov observatory was utilized). The reason for the cluster optimization is the higher time demands of these pipelines. In the case of the downloading pipeline, it is because of the usually large amount of data to be downloaded (one 24-hour observation results in approximately 33 GB of data). For the datacube pipeline, the reason is computational time, where a 24-hour observation took around 25 minutes to be computed on the Ondřejov setup, and computational power demand where each 24 datacube blocks 1 CPU core and takes up to around 10 GB of RAM. This would require the jobs to be run sequentially on most local machines while on most clusters, where RAM is usually not an issue, more jobs can be run concurrently leading to saving considerable amounts of time.

A high-level flowchart of the folder structure preparation pipeline is shown in Fig. 5.4. Initially, the configuration is loaded. This configuration contains DRMS request strings, a path to the data (if already downloaded), origin latitudes and longitudes in Carrington coordinates, lower and upper limits for implanted velocities, and the velocity sample count. The implanted velocities are randomly sampled within the given velocity bounds. Subsequently, an iteration over all requests occurs, where for each request, we check if its data are already downloaded. If not, a new folder is prepared for the data and the request is stored in a helper file that will be used as an input for the following data download pipeline. Then, for the given request, we iterate over all injected velocities, and for each (request, velocity) pair, a new folder structure for the final datacube is prepared, along with all necessary configuration files for the tracking pipeline and the travel-time pipeline.

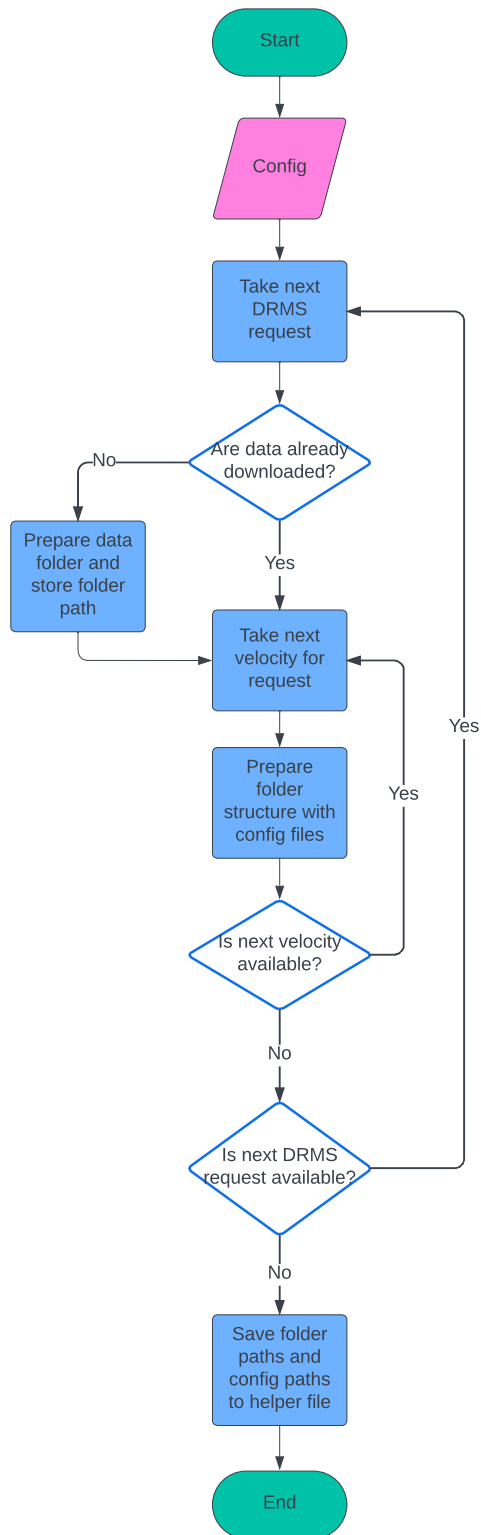


Figure 5.4: High-level flowchart of the folder preparation pipeline. It contains two nested iterations; the outer one over all provided DRMS requests and the inner one over all randomly sampled injected velocities.

The data download pipeline (step 2 in the initial enumeration of this section) is needed only in case some data provided in the configuration of the folder structure preparation pipeline are not yet downloaded. In that case it is expected that the respective helper file is non-empty and contains JSOC DRMS requests for the data to be downloaded. The process is then shown in Fig. 5.5. First, there is an assert check for non-emptiness of the helper file. If the file indeed contains some data an iteration over each request in the file occurs. For each request, a DRMS download query is created and executed and the downloaded data, Dopplergrams in FITS format, are stored to the folder specified in the config. After a successful download the request entry is remove from the helper file.

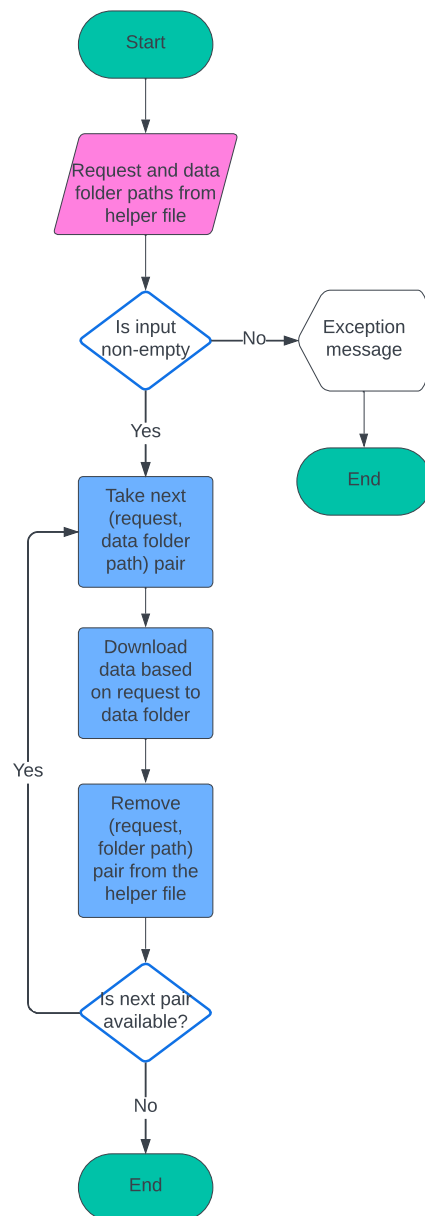


Figure 5.5: A high-level flowchart of the data download pipeline. It serves as an optional middle step between the folder preparation pipeline and the tracking pipeline in cases where not all Dopplergrams are present on the local storage.

The last and arguably the most important part of the process is the tracking pipeline depicted in Fig. 5.7. Its job is to convert a series of Dopplergrams (in our case, 6-hour observations were used) into a datacube containing data from the tracked area with an additional velocity perturbation from the artificially implanted velocity of the tracked area. The pipeline starts by reading a configuration JSON file created in the folder structure preparation pipeline (step 1). This configuration file contains the following parameters:

- A path to the folder containing the data (Dopplergrams)
- Projection origin in Carrington coordinates (this origin is applied to the frame in the middle of the time series while the rest are shifted according to the implanted velocity and time difference from the middle frame)
- The shape of the tracked area in pixels (consequently, the shape of each output frame in pixels); value used for all projections: [512, 512]
- Time step between consecutive Dopplergrams in seconds; value used for all projections (given by the observation): 45 s
- Scaling of the output frame in heliographic degrees per pixel; value used for all projections: [0.12, 0.12]
- Radius of the Sun in megameters (necessary for a correct projection); value used for all projections: 696.0 Mm
- Artificial (implanted) longitudinal velocity in meters per second
- Filename for the output datacube FITS file

First, the pipeline lists all the FITS files present in the provided data folder (we implicitly presume that all Dopplergrams are in FITS format as it is a common standard), sorted by the date of observation encoded in the name of each file. Then, an empty array with dimensions $(t, x, y) = (\text{file count}, x \text{ shape from config}, y \text{ shape from config})$ is created. This array will eventually contain the projected data from the tracked area. Further, an iteration over the sorted files occurs. In each iteration, the origin of the projection for the selected frame is computed based on the implanted velocity and the time difference between the frame and the middle frame. Then, data from the file are read, and only the part inside the tracked area – a rectangle given by its shape and scaling from the config – is selected, and the Postel projection is applied to this data. This process is shown in Fig. 5.6. In order to avoid blank pixels that might appear as a result of the projection, all NaN values are replaced by the median of all non-empty values. As a last step for a given frame, a quadratic surface is subtracted to remove the effect of solar rotation from the data. This process is repeated for each Dopplergram, while all projected tracked area frames are appended to the output array. After the iteration is complete, the output array (datacube) is saved into a new FITS file with a name specified in the initial configuration file.

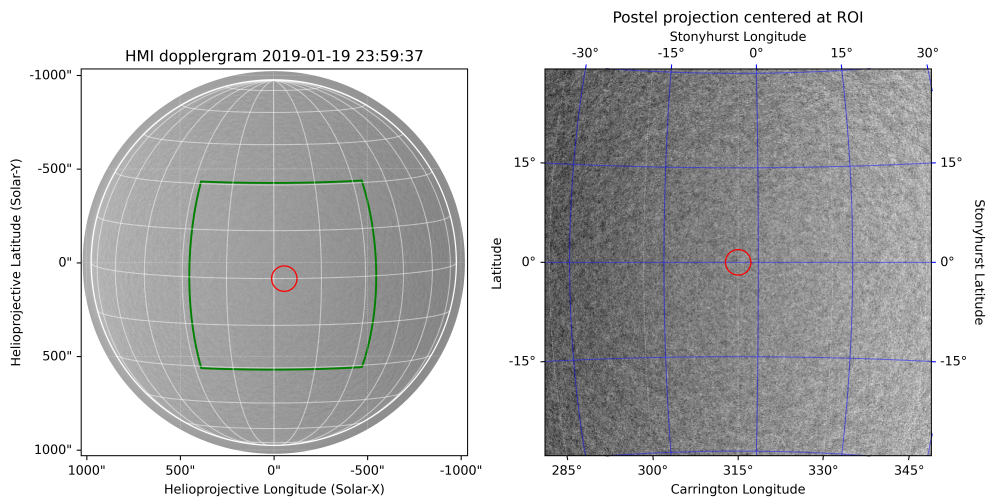


Figure 5.6: Left: HMI Dopplergram in helioprojective coordinates with the area of selection highlighted in green. Right: Selected area in Carrington and Stonyhurst coordinates after application of the Postel projection.

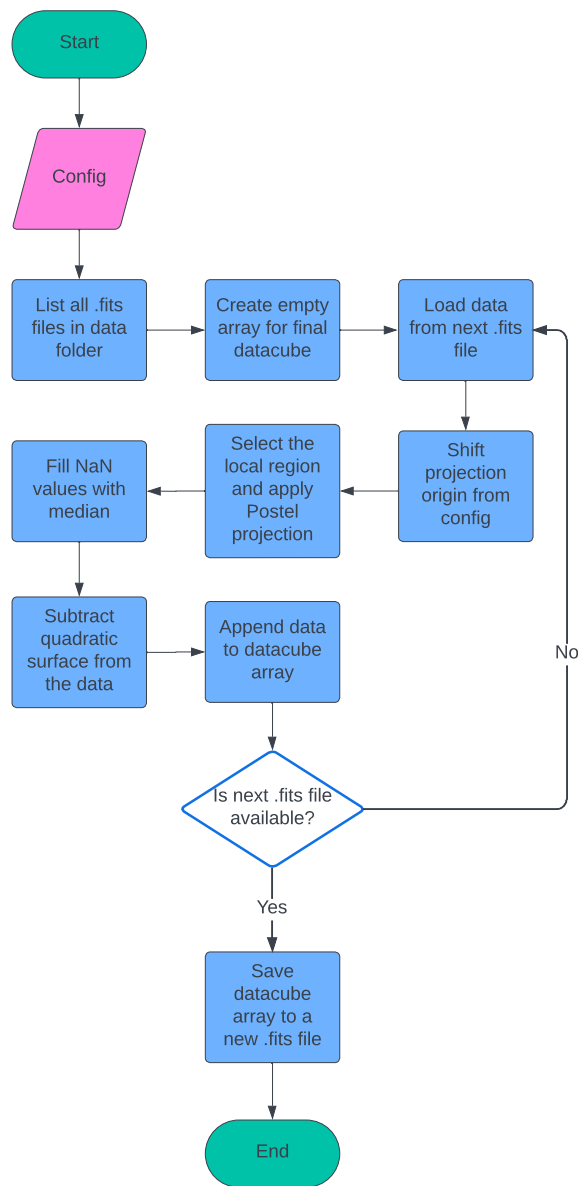


Figure 5.7: High-level flowchart of the tracking pipeline. It lists all FITS files (containing Dopplergrams) present in the provided folder path, sorted by date encoded in their name, and iterates over them. In each iteration a shift, determined by the injected velocity and time difference between the frame and central frame, is applied to the origin; tracked area is selected and the Postel projection is applied on it. Further, NaN values are replaced by a median of all values and quadratic surface is subtracted from the data, removing the effect of solar rotation. The processed frame is appended to a datacube array. After the iteration is complete, the datacube array is stored in a new FITS file.

5.5 Travel-time pipeline

In general, measurements of helioseismic travel times consist of three consecutive steps. The travel-time pipeline operated on the data-processing computer cluster at the Astronomical Institute of the Czech Academy of Sciences in Ondřejov is no exception.

First, the input datacube—the output of the tracking pipeline—is detrended over time, and a mean frame (average of the frames over time) is subtracted. This step removes existing large-scale trends in the observations, such as the residual signal from the differential rotation and stable velocity features, like most of the signal from solar supergranules.

Next, the detrended datacube is apodized in both space and time. This is necessary because subsequent calculations are performed in Fourier space, which implicitly assumes periodic boundary conditions that are not met in reality. Apodization with a smooth function at the edges helps to mitigate this issue. The apodization is applied to 5% of the pixels and frames at the boundaries.

Then, the datacube is transformed to Fourier space. We obtain a datacube with the same dimensions but with axes (k_x, k_y, ω) , where k_x and k_y represent the horizontal components of the wave vector, and ω represents the angular frequency. Representing the datacube in Fourier space is convenient for applying various $k - \omega$ filters. During this step, plots of the data power spectrum are created for potential later visual inspection.

After preprocessing the input datacube, filtering is performed simply by multiplying the Fourier representation of the datacube with a constructed travel-time filter. Following the literature on the subject, both ridge filters and phase-speed filters are applied. The result of this task is a filtered datacube, one for each $k - \omega$ filter.

These filtered datacubes are inputs for the travel-time measurements procedure. This task may be divided into several consecutive sub-steps. First, a spatial averaging filter representing the travel-time measurements geometry is applied. In this study, we only considered annulus filters with a radius corresponding to the distance of cross-correlated points. For studying the travel-time integrals, the geometry considering the propagation of the waves in the east-west direction was the most significant. This is mimicked by an annulus with a Gaussian lateral profile, multiplied by the sine of the horizontal phase angle. The observations to the west of the central point are weighted positively, and those to the east negatively. This geometry is sensitive to the flows in the east-west direction. Spatial averaging over the annulus increases the signal-to-noise ratio compared to hypothetical point-to-point measurements.

The signal at the central point is then cross-correlated with the signal averaged over the (weighted) surrounding annulus. The map of cross-covariances (for a series of time lags with critical sampling) is stored. Then, the travel times that minimize the cross-covariance of the signals at the given point are measured. In reality, positive and negative travel times are computed separately (positive travel times indicate the travel of waves from the central point to the surrounding

annulus, whereas negative travel times represent the opposite direction). It is noted in the literature (Burston et al., 2015) that *differences* between these two travel times are most sensitive to the flows. Both positive and negative travel times are stored separately in the output files.

The above-described workflow was implemented in a pipeline coded in the MATLAB language. Each of the three steps is represented in a separate module. MATLAB allows for the compilation of the code into binaries, which can then be executed in the compute cluster environment. The workflow was adapted to be used within a PBS/Torque job management system running at a small compute cluster in Ondřejov. It involves proper allocation of resources given the size of the input datacube and also processes obvious job dependencies within consecutive steps. The code is versatile and uses a text-based configuration file to implement various options that might be useful for different tasks. This includes potential further spatial averaging to reduce random noise, different definitions of travel-time measurements, and the possible selection of a reference cross-covariance in the case of linearized travel-time definitions.

6. Results

Despite being primarily a stepping stone for obtaining the main results presented later, building the tracking pipeline, as detailed in Sec. 5.4, was one of the pivotal aspects of this work. The pipeline enables users to download data (Dopplergrams) from JSOC, open them, and create datacubes that serve as inputs for the standard travel-time pipeline described in Sec. 5.5. A feature essential for our objectives, which is absent in similar pipelines, is the capability to inject a constant longitudinal velocity flow into the data. This pipeline is implemented in Python using libraries such as SunPy, Astropy, and DRMS, and is available in the GitHub repository <https://github.com/YoungMasterGandalf/thesis-work>.

The practical part of this work can be described surprisingly succinctly, given that the methodologies and pipelines used have already been elaborated upon in previous chapters. We initiated the process by selecting a few days of observations with minimal magnetic activity. This is crucial because, as mentioned in Sec. 3.2.2, our analysis assumes only the presence of small perturbations. During periods of high magnetic activity, the likely inclusion of one or more sunspots in the tracked area would violate this assumption.

All observational data used in this work, consisting of a series of Dopplergrams captured by the SDO’s HMI instrument, were utilized as input data. The configurations of these Dopplergram sequences are detailed in Table 6.1. Other observation configurations were employed during the testing of the tracking pipeline and the overall process described in Chap. 4, Methodology; however, these were not listed as they were not part of the final batch of data presented in the results.

Table 6.1: Dopplergram configurations utilized in this thesis. T represents the observation time in hours, while ΔT denotes the cadence (the time between two consecutive frames) in seconds. Origin lon./lat. are Carrington coordinates of the projection origin of the middle frame in the sequence. The number of datacubes corresponding to the provided Dopplergram sequence (# datacubes) is determined by the number of injected velocities for the given configuration.

Date	Origin lon. (°)	Origin lat. (°)	T (h)	ΔT (s)	# images	# datacubes
03/12/2017	280	0	6	45	482	54
05/12/2017	200	0	6	45	482	74
08/13/2017	40	0	6	45	482	75
10/08/2017	30	0	6	45	482	75
11/03/2017	40	0	6	45	482	75
12/01/2017	40	0	6	45	482	75
03/26/2018	310	0	6	45	482	75
01/20/2019	315	0	6	45	482	75
01/20/2019	315	-20	6	45	482	63
01/20/2019	315	20	6	45	482	75

Configuration files and folder structures were created by running the preparation pipeline shown in Fig. 5.4. For each combination of observation date and projection origin, 75 datacube configurations were prepared, each with a different injected velocity. These velocities were randomly sampled from the sequence $-500, -499, \dots, 499, 500 \text{ ms}^{-1}$. The data were subsequently downloaded from JSOC using the pipeline depicted in Fig. 5.5. As a result, 600 datacube configurations were prepared at 0° latitude, 75 at 20° latitude, and 75 at -20° latitude.

Next, the tracking pipeline (Fig. 5.7) and the travel-time pipeline were run synchronously for each configuration. Synchronous execution means that the travel-time pipeline commenced only after the completion of the tracking pipeline, as it relies on the datacubes generated by the tracking process as input. The execution was managed in batches on the Ondřejov Observatory compute cluster to avoid overloading the job management system. Each batch corresponded to one observation date, encompassing 75 injected velocities. The discrepancy in the number of datacubes shown in Tab. 6.1 arises because some jobs unexpectedly failed, most likely due to errors in the cluster's job management system. However, the number of failed jobs was not substantial enough to significantly compromise the quality of the validation, leading us to proceed with the successfully processed data. Ultimately, 578 datacubes at 0° latitude were generated and processed by the travel-time pipeline, along with 63 at -20° latitude and 75 at 20° latitude.

Each datacube processed by the travel-time pipeline yields, among other outputs, travel-time perturbation maps for various filters and annulus radii. The combinations of filters and annulus radii, expressed in pixels, include:

- Ridge filters:
 - f: [5, 6, 7, 8, 9, 10, 11, 12, 13, 14, 15, 16, 17, 18, 19, 20] (px)
 - p1: [5, 6, 7, 8, 9, 10, 11, 12, 13, 14, 15, 16, 17, 18, 19, 20] (px)
 - p2: [5, 6, 7, 8, 9, 10, 11, 12, 13, 14, 15, 16, 17, 18, 19, 20] (px)
 - p3: [5, 6, 7, 8, 9, 10, 11, 12, 13, 14, 15, 16, 17, 18, 19, 20] (px)
 - p4: [5, 6, 7, 8, 9, 10, 11, 12, 13, 14, 15, 16, 17, 18, 19, 20] (px)
- Phase speed filters:
 - td1: [2.5, 3.4, 4.2, 5.1, 6] (px)
 - td2: [4.2, 5.1, 6, 6.8, 7.7] (px)
 - td3: [6, 7, 7.9, 8.9, 9.9] (px)
 - td4: [9.9, 10.8, 11.6, 12.4, 13.3] (px)
 - td5: [13, 15, 17, 18, 20] (px)
 - td6: [18, 19, 21, 22, 24] (px)
 - td7: [22, 23, 25, 27, 29] (px)
 - td8: [26, 28, 29, 31, 33] (px)
 - td9: [30, 32, 34, 35, 37] (px)
 - td10: [35, 36, 38, 39, 41] (px)
 - td11: [39, 40, 42, 44, 46] (px)

We continued with the validation process as outlined in Chap. 4, Methodology. For each filter and geometry, we created plots comparing mean travel-time perturbations against injected velocities. Examples of these plots, generated from datasets originating at 0° latitude for various modes and geometries, are displayed in Fig. 6.1.

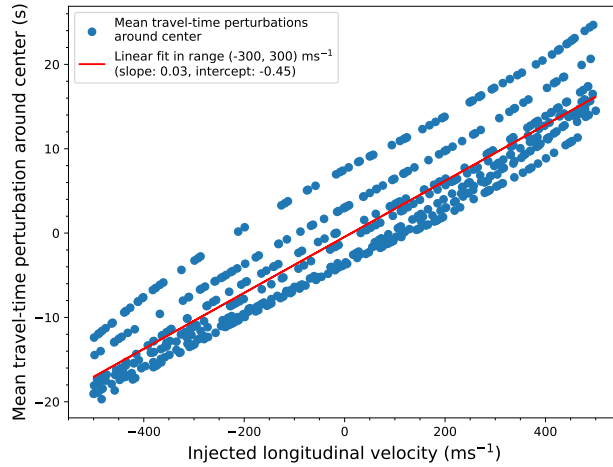
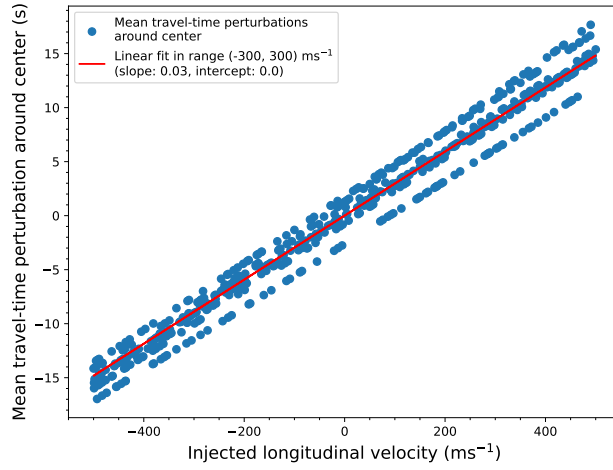
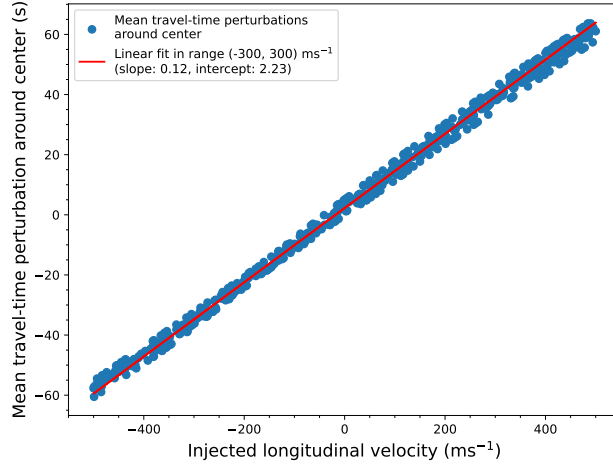


Figure 6.1: Mean travel-time perturbation around center vs. injected velocity plots created from the dataset with the latitude of the tracked area origin equal to 0° and the following configurations: f mode, e-w geometry, $\Delta = 10$ px (top); p3 mode, e-w geometry, $\Delta = 15$ px (middle); td11 (phase speed filter), e-w geometry, $\Delta = 46$ px (bottom).

A distinct separation is evident in the data, particularly for modes that penetrate deeper into the Sun. Each plot appears to showcase a series of linear relationships with similar slopes but vertically offset from each other. This phenomenon is attributed to each line representing data from a different observation date for the specified configuration. It has been documented by several researchers (Basu and Antia, 2019; Li et al., 2013; Mordvinov and Plyusnina, 2000, and others) that the solar rotation is not constant but varies periodically over time. Any deviation in solar rotation from the Carrington rotation contributes to the average background perturbation term discussed in Eq. 4.5. This factor varies across different observation dates and configurations. Notably, this issue does not affect the datasets at latitudes 20° and -20° , as these were derived from a single observation date.

Fitting data with such inherent variability is problematic, as it may lead to a biased trend. To address this, we segregated the dataset by observation dates and generated the same plots for all configurations, but separately for each observation date. A new set of example plots, derived from the dataset dated 01/20/2019 at 0° latitude, is illustrated in Fig. 6.2.

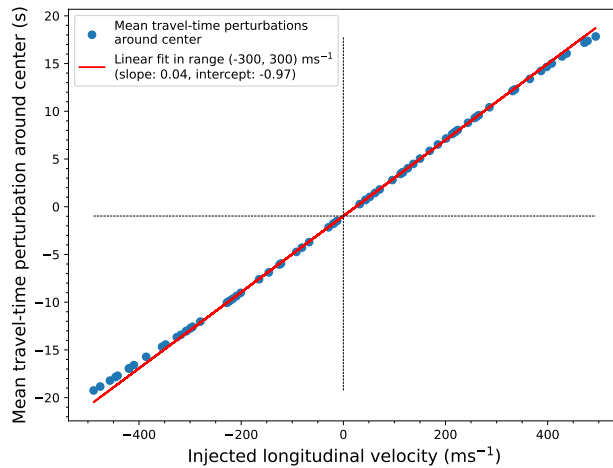
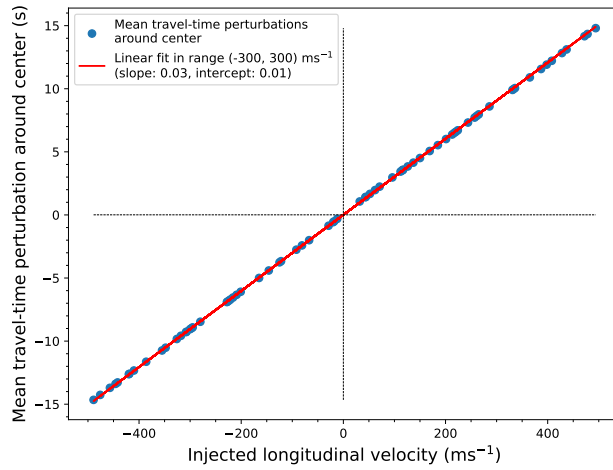
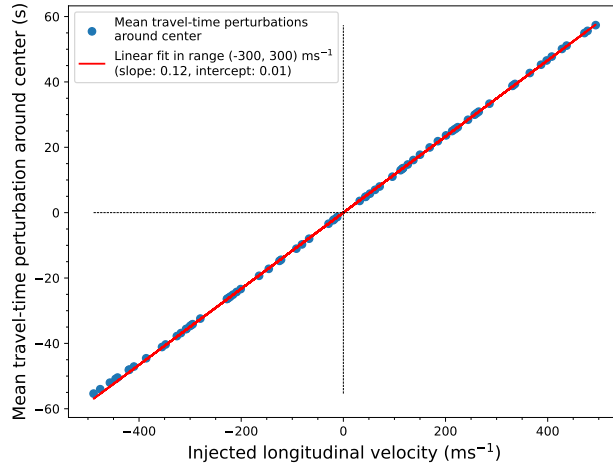


Figure 6.2: Mean travel-time perturbation around center vs. injected velocity plots created from a single observation date, 01/20/2019, tracked area origin latitude equal to 0° and the following configurations: f mode, e-w geometry, $\Delta = 10$ px (top); p3 mode, e-w geometry, $\Delta = 15$ px (middle); td4 (phase speed filter), e-w geometry, $\Delta = 9.9$ px (bottom).

For each configuration (filter and annulus radius), we obtained eight slopes and their corresponding errors from eight observation dates. To derive a single slope per configuration, we calculated the weighted averages of the slopes and their errors for each observation date using the formula outlined in (Taylor and Thompson, 1982):

$$x_{\text{wav}} = \frac{\sum_i w_i x_i}{\sum_i w_i} , \quad (6.1)$$

where the sums are over all observation dates, i.e., $i = 1, \dots, 8$, and the weights w_i are reciprocal values of the corresponding uncertainties

$$w_i = \frac{1}{\sigma_i^2} . \quad (6.2)$$

The final uncertainty of the weighted average x_{wav} is

$$\sigma_{\text{wav}} = \frac{1}{\sum_i \sqrt{w_i}} , \quad (6.3)$$

where again $i = 1, \dots, 8$.

The datasets at latitudes 20° and -20° were primarily processed to test the effect of differential rotation on the resulting data. Similar to the variable solar rotation observed on different dates, the differential rotation velocities at lower and higher latitudes were not expected to alter the slopes of the graphs, but rather to introduce an additional vertical shift. This hypothesis was confirmed, as illustrated in Figures 6.3, 6.4, and 6.5.

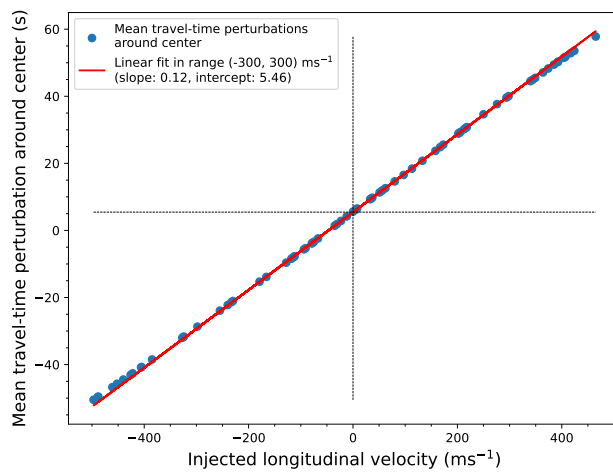
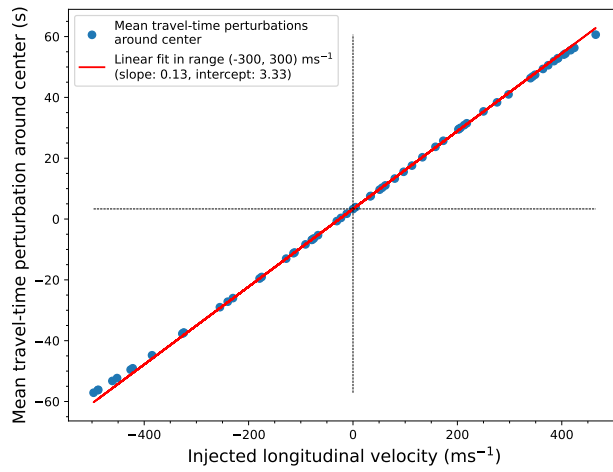
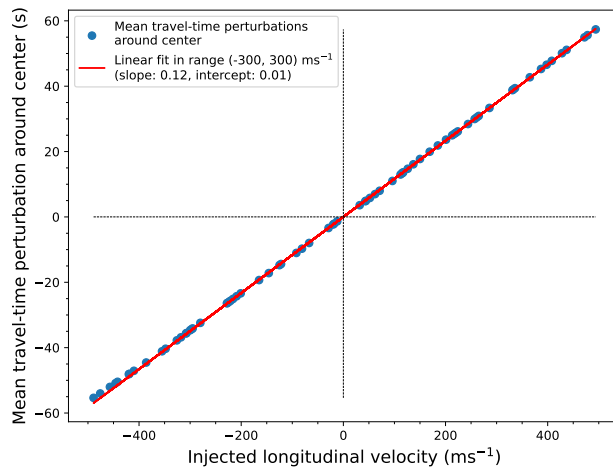


Figure 6.3: Mean travel-time perturbation around center vs. injected velocity plots created from a single observation date, 01/20/2019, for the configuration: f mode, e-w geometry, $\Delta = 10$ px. The difference in configurations was the tracked area origin latitude: 0° (top), -20° (middle), 20° (bottom).

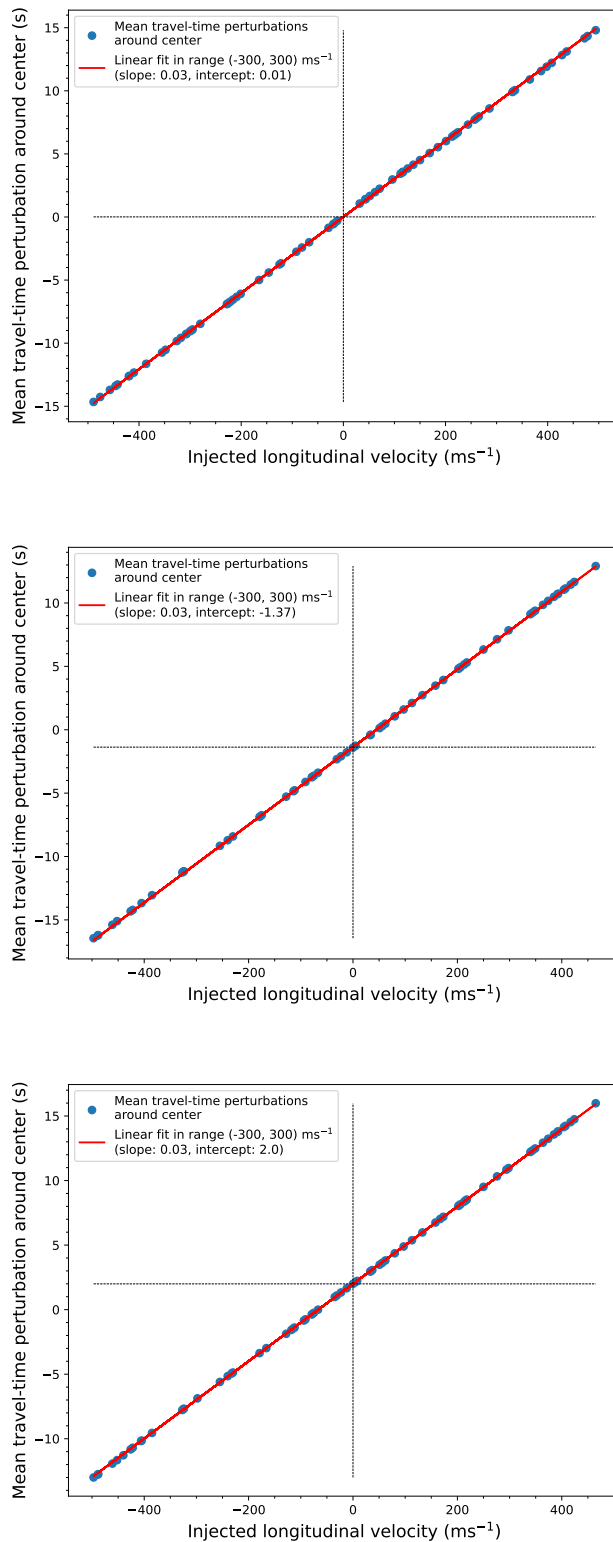


Figure 6.4: Mean travel-time perturbation around center vs. injected velocity plots created from a single observation date, 01/20/2019, for the configuration: p3 mode, e-w geometry, $\Delta = 15$ px. The difference in configurations was the tracked area origin latitude: 0° (top), -20° (middle), 20° (bottom).

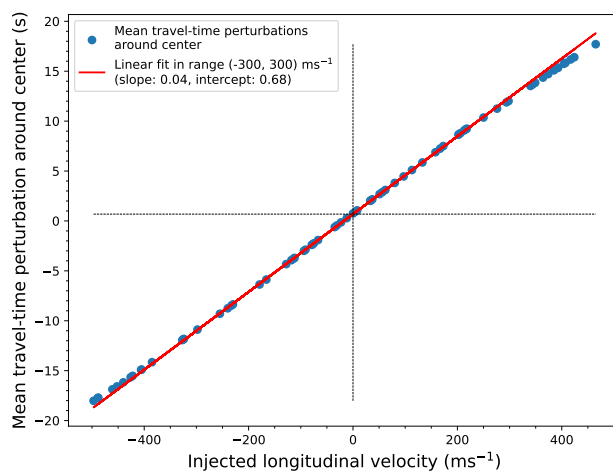
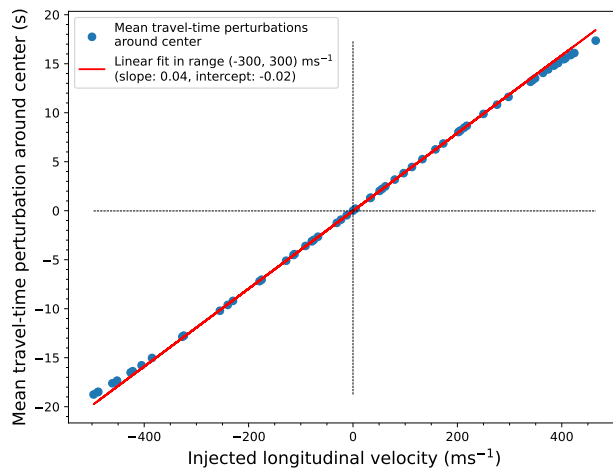
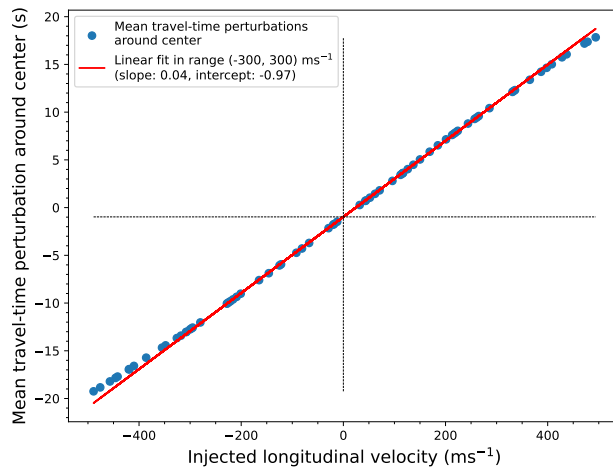


Figure 6.5: Mean travel-time perturbation around center vs. injected velocity plots created from a single observation date, 01/20/2019, for the configuration: td4 (phase speed filter), e-w geometry, $\Delta = 9.9$ px. The difference in configurations was the tracked area origin latitude: 0° (top), -20° (middle), 20° (bottom).

The final step of our validation method, as outlined in 4, Methodology, involved comparing the slopes of the linear regressions from all graphs with the volume integrals of velocity perturbation kernels for corresponding filters and geometries, as calculated from the models. As explained in the aforementioned chapter, specifically in Eq. 4.5, these slopes represent the same quantity obtained through a model-independent method. The results for the primary dataset at 0° latitude are displayed in Fig. 6.6.

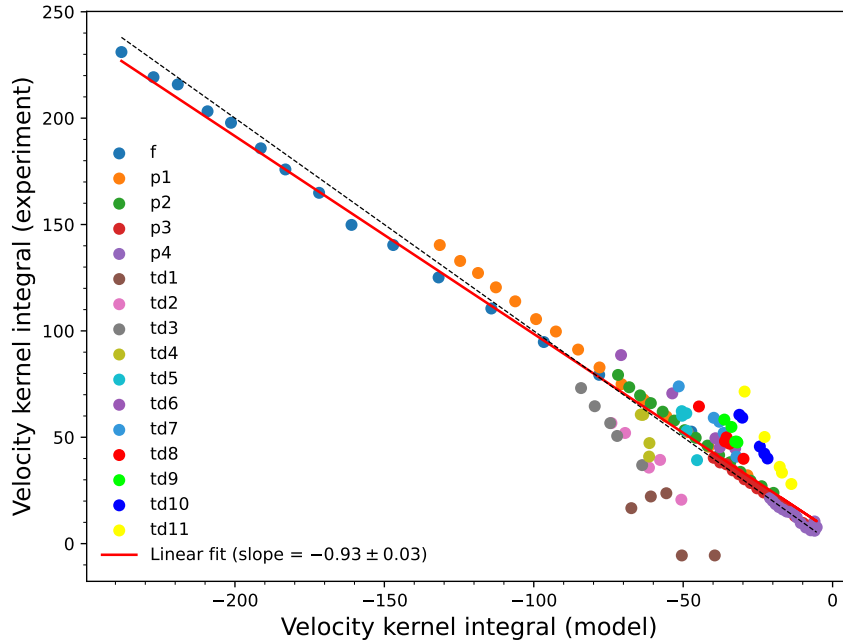


Figure 6.6: Volume integrals of velocity perturbation kernels obtained from linear regression slopes (model independent) vs. volume integrals of the velocity perturbation kernels calculated from forward modelling. The data were obtained from the dataset containing 8 observation dates with the origin latitude of the tracked area equal to 0° for various ridge and phase speed filters.

The data were then organized and plotted with filters of the same type grouped together, specifically, $\{p1, \dots, p4\}$ grouped as p modes and $\{td1, \dots, td11\}$ as td modes. The results of this grouped filters are displayed in Fig. 6.7.

Similar results were obtained for the 20° and -20° datasets and are shown in Fig. 6.8.

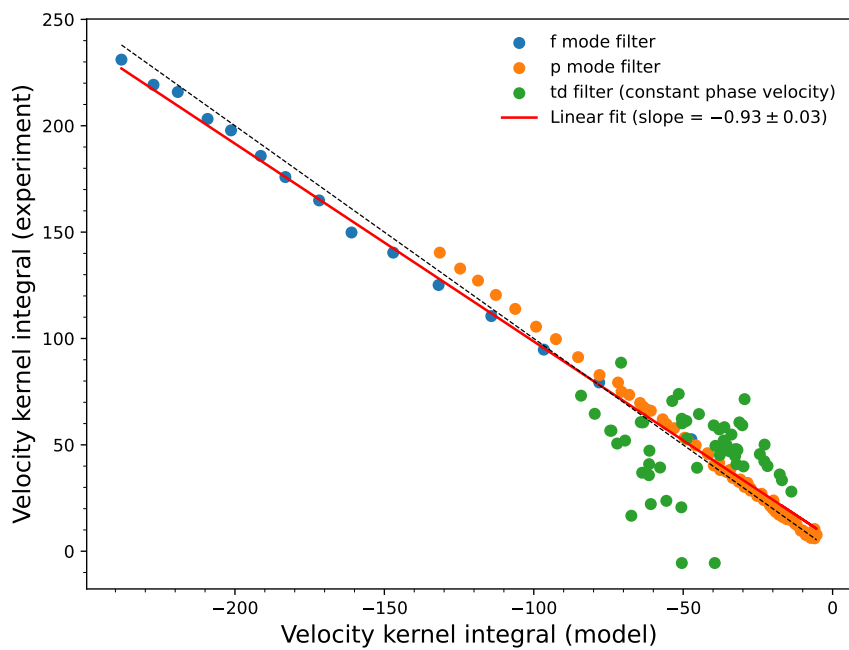


Figure 6.7: Volume integrals of velocity perturbation kernels obtained from linear regression slopes (model independent) vs. volume integrals of the velocity perturbation kernels calculated from forward modelling. The data were obtained from the dataset containing 8 observation dates with the origin latitude of the tracked area equal to 0° for various ridge and phase speed filter groups.

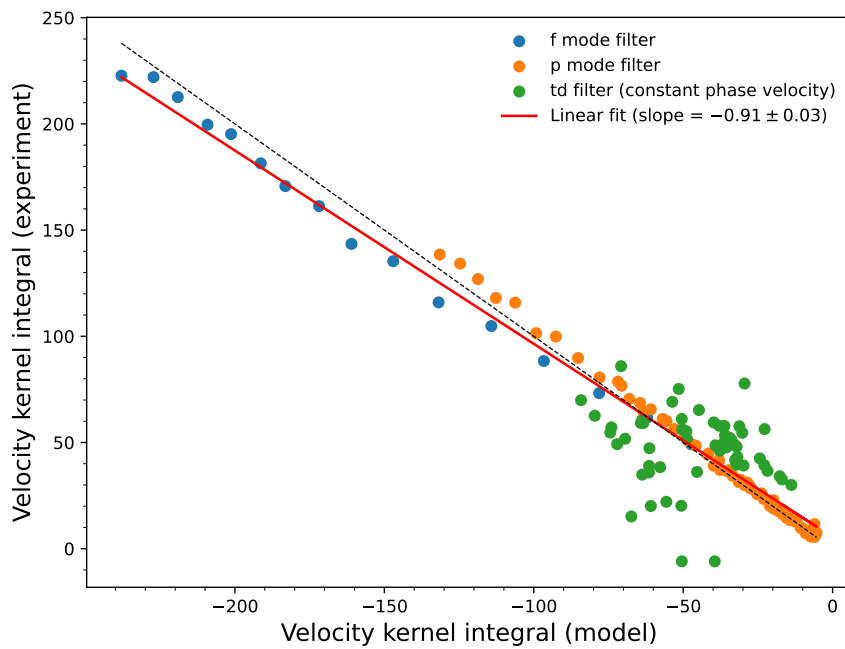
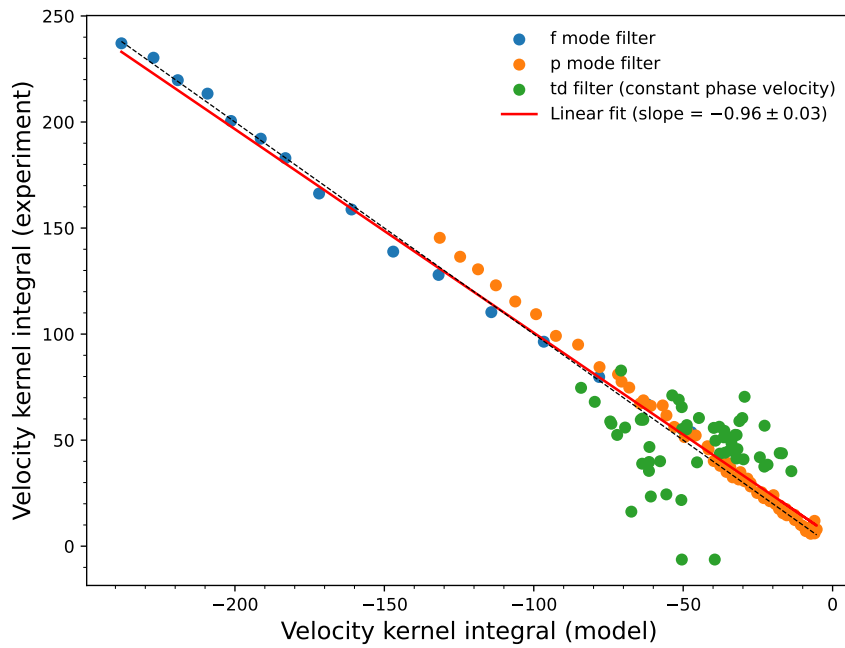


Figure 6.8: Volume integrals of velocity perturbation kernels obtained from linear regression slopes (model independent) vs. volume integrals of the velocity perturbation kernels calculated from models. The data were obtained from the dataset containing 8 observation dates with the origin latitude of the tracked area equal to -20° (top) and 20° (bottom) for various ridge and phase speed filter groups.

7. Discussion

The principal findings of this thesis are presented in Figures 6.6 and 6.7. The results demonstrate that the volume integrals of the velocity perturbation sensitivity kernels, obtained using our proposed model-independent method, align well with those calculated from models for ridge filters f and $p1 - p4$. This alignment is underscored by the slope of the linear fit: -0.93 ± 0.03 , and further solidified by Pearson's correlation coefficient (Pearson, 1895) for these filters, which stands at $\rho_{f/p} = -0.999$, indicating a strong linear correlation. Conversely, the results for the phase speed filters $t1 - t11$ do not exhibit a similar correlation; the volume integrals of the sensitivity kernels show very little similarity to their model counterparts, as evidenced by Pearson's coefficient $\rho_{td} = -0.198$, suggesting virtually no linear correlation. The negative sign in both the slopes and correlation coefficients arise from the chosen sign convention of the injected velocity. This velocity, featured in Figures 6.1, 6.2, 6.3, 6.4, and 6.5, represents the velocity of the frame which artificially induces a flow of the same magnitude but in the opposite direction, as detailed in Chap. 4.

These findings lead to the conclusion that phase speed filtering may yield unreliable results, a notion previously suggested by other researchers by observing inconsistencies in their inversions (Švanda, 2015; DeGrave and Jackiewicz, 2015).

Further discussion in this chapter explores various factors that might potentially influence the results, demonstrating that they either had no effect or were appropriately accounted for.

7.1 Injected velocity flow vs. real flow

One potential question concerns whether the injected longitudinal velocity truly results in an artificial flow within the data. To address this, ring diagrams were constructed. As detailed in Sec. 3.1 and supported by the literature (Christensen-Dalsgaard, 2002; Kosovichev, 2011), the presence of a horizontal flow in the tracked area is indicated in the ring diagram by a distortion of the ring pattern—specifically, the rings will not be concentric if any horizontal flow is present. A ring diagram for a test configuration with an injected velocity of $v_0 = 500$ m/s compared to a one with no injected velocity is shown in Fig. 7.1. It qualitatively demonstrates the presence of a horizontal flow, as evidenced by the horizontal distortion of the rings visible in the bottom diagram.

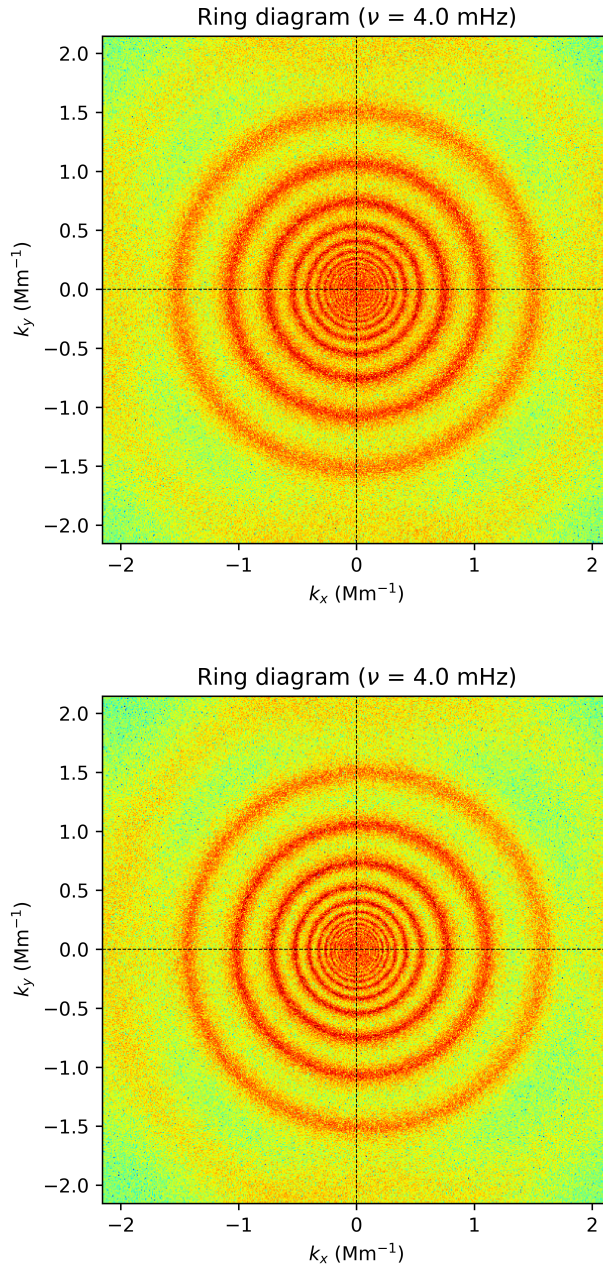


Figure 7.1: Ring diagrams created from power spectra of a 24-hour observation at $\nu = 4$ mHz. The upper diagram corresponds to a dataset with no injected velocity resulting in all rings being concentric circles. The bottom diagram was created from a dataset with an injected horizontal velocity $v_0 = 500$ m/s resulting in the visible horizontal distortion of the rings.

A direct comparison of the horizontal velocity with the injected one is also possible. In the Dopplergrams, the indication for the large-scale convective cells of supergranulation (Rincon and Rieutord, 2018) are clearly visible. The supergranular structures therefore can be used to determine the horizontal flow field on the solar surface (e.g. Švanda et al., 2006, and the follow-up papers). Such goal may be achieved by applying the method of local correlation tracking (LCT; November, 1986) to Dopplergram datacubes.

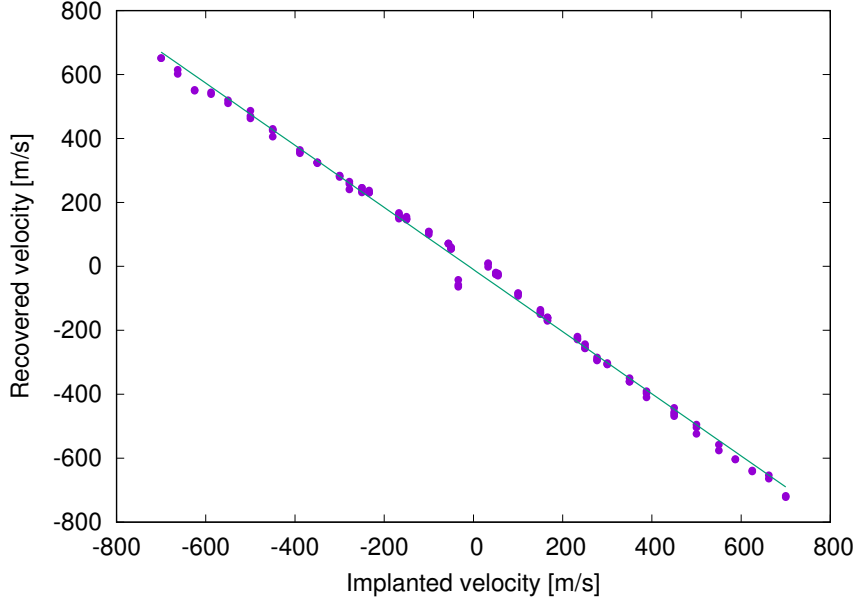


Figure 7.2: Comparison of the implanted velocity and the horizontal velocity determined from the manipulated datacubes using a LCT algorithm.

The local correlation tracking algorithm searches for the optimal displacement that minimises the differences of the floating spatial windows capturing slowly evolving features in the time sequence. Knowing the sampling of the cross-correlated frames, the detected displacement may be converted to the horizontal velocity vector.

The results of the testing of our pipeline are shown in Fig. 7.2. The measured surface horizontal velocities obviously very well correspond to the implanted velocity, thereby validating the performance of the tracking pipeline.

7.2 Observation times

Another tested factor was the observation time. Initially, 24-hour sequences were examined during the testing phase of the tracking pipeline. After confirming the stability and expected functionality of the pipeline, 6-hour sequences were employed as inputs, and the outcomes were compared. Since the results obtained from the 24-hour sequence inputs were identical to those from the 6-hour sequence inputs, we opted to utilize 6-hour sequences for the primary data batch to expedite processing.

7.3 GB02 vs. GB04

Differences between GB02 and GB04 are detailed in Sec. 3.2.1 and further explored in (e.g. DeGrave et al., 2014). Initially, the tracking pipeline was exclusively tested using GB04, as it requires less computational time for the specified task compared to GB02. However, GB02 demonstrates better stability in non-linear regions, particularly for higher flow velocities (DeGrave et al., 2014).

This non-linear behavior is evident in e.g., Fig. 6.5, where the outer values clearly deviate from a linear trend. Consequently, all regressions were conducted within the linear velocity range of $(-300, 300)$ m/s. Since the regressions were confined to this linear region, there was no significant difference between using GB02 or GB04 in terms of the final results. Nevertheless, due to its superior stability, GB02 was selected for the main processing run.

7.4 Differential rotation

Considering the size of the tracked area, which has dimensions of 512×512 pixels and a scaling of $0.12^\circ/\text{px}$, results in a roughly $60^\circ \times 60^\circ$ spherical rectangle, it is essential to evaluate the potential effects of differential rotation. As previously discussed in Chap. 6, Results, we hypothesized that the discrepancy between the actual solar rotation at the given location and the Carrington rotation applied would only manifest within the background perturbation term, as outlined in Eq. 4.5.

This assumption was tested by comparing the mean travel-time perturbation versus injected velocity plots for identical observation dates and configurations across different latitudes of the tracked areas' origins. The results are depicted in Figures 6.3, 6.4, and 6.5. As observed, the linear dependence remains consistent across all latitudes for the specified configurations, while only the intercept varies. Thus, differential rotation manifests solely as a vertical shift in these dependencies, thereby not affecting the overall results presented.

7.5 Reference cross-covariance

The significance of selecting an appropriate reference cross-covariance C_0 was briefly discussed in Sec. 3.2.1, with the primary objective being to minimize the contribution of the group travel time to the results. It was also noted that in some instances, the reference cross-covariance derived from the forward model might not be sufficiently accurate. This issue arose during our work. Initially, in the testing phase, the travel-time pipeline consistently used a cross-covariance that had been pre-calculated from forward modeling. Similar to the GB02 versus GB04 discussion, this approach is advantageous in terms of computational efficiency.

However, the resulting data, after evaluating all other potential influences detailed in this chapter, were demonstrably incorrect. It became clear that in our case, the pre-calculated cross-covariance was not sufficiently precise. Additionally, there might have been a secondary source of inaccuracy related to the injected flows. Without systematic flows, the point of wave emergence is centered within a given pixel. However, the introduction of a systematic flow might slightly shift the emergence point, causing an overlap with neighboring pixels. Both of these issues were addressed by constructing the cross-covariance for each travel-time pipeline setting as a spatial average over the field of view in the selected region. Such an averaging to obtain the reference cross-covariance is not novel and is being used quite often in the community.

Conclusion

This thesis investigated the feasibility of a model-independent approach to determine the volume integrals of velocity perturbation kernels using travel-time measurements from helioseismic data. The core methodology involved injecting a controlled longitudinal flow into Dopplergrams datacubes and subsequently analyzing the resulting travel-time perturbations.

The key findings are summarized in Figures 6.6 and 6.7. The results demonstrate a strong correlation between the volume integrals of velocity perturbation kernels derived from the model-independent method and those calculated from forward models for ridge filters (f and p1–p4). This is supported by the linear fit slope of -0.93 ± 0.03 and a Pearson’s correlation coefficient of $\rho_{f/p} = -0.999$ (the negative signs are consequences of the chosen convention). In contrast, the phase speed filters (td1 – td11) exhibited a weak correlation ($\rho_{f/p} = -0.198$) between the two sets of volume integrals, suggesting that phase speed filtering might not be a reliable approach for this purpose.

These findings align with prior research suggesting potential issues with phase speed filtering. The discussion chapter further explores potential influencing factors and demonstrates that they were either negligible or adequately accounted for. Additionally, ring diagrams and an LCT algorithm confirmed the presence of an artificial flow within the data due to the injected velocity.

In conclusion, this thesis tested the validity of volume integrals of velocity perturbation kernels with a model-independent method. The method showed high correlation with model kernels for ridge filters f and p1 – p4. On the other hand, strong inconsistencies were observed for phase speed filters, td1 – td11, showing almost no correlation with model kernels. This results suggest that there might be issues in kernel calculation methods employed by various models.

Bibliography

- Xu Zhen-tao. The hexagram “feng” in “the book of changes” as the earliest written record of sunspot. *Chinese Astronomy*, 4(4):406, 1980. ISSN 0146-6364. doi: [https://doi.org/10.1016/0146-6364\(80\)90034-1](https://doi.org/10.1016/0146-6364(80)90034-1). URL <https://www.sciencedirect.com/science/article/pii/0146636480900341>.
- J.M. Vaquero. Historical sunspot observations: A review. *Advances in Space Research*, 40(7):929–941, 2007. ISSN 0273-1177. doi: <https://doi.org/10.1016/j.asr.2007.01.087>. URL <https://www.sciencedirect.com/science/article/pii/S0273117707004747>.
- Robert B. Leighton, Robert W. Noyes, and George W. Simon. Velocity Fields in the Solar Atmosphere. I. Preliminary Report. *ApJ*, 135:474, March 1962. doi: 10.1086/147285.
- Roger K. Ulrich. The Five-Minute Oscillations on the Solar Surface. *ApJ*, 162: 993, December 1970. doi: 10.1086/150731.
- J. W. Leibacher and R. F. Stein. A New Description of the Solar Five-Minute Oscillation. *Astrophys. Lett.*, 7:191–192, January 1971.
- Gaël Buldgen. Global helioseismology. *arXiv preprint arXiv:1912.02003*, 2019.
- Rafael A. García, Sylvaine Turck-Chièze, Sebastian J. Jiménez-Reyes, Jérôme Ballot, Pere L. Pallé, Antonio Eff-Darwich, Savita Mathur, and Janine Provost. Tracking solar gravity modes: The dynamics of the solar core. *Science*, 316 (5831):1591–1593, 2007. doi: 10.1126/science.1140598. URL <https://www.science.org/doi/abs/10.1126/science.1140598>.
- Hathaway, D. H. NASA/Marshall Solar Physics, 2022. URL <https://solarscience.msfc.nasa.gov/>.
- E. E. Salpeter. Nuclear reactions in the stars. i. proton-proton chain. *Phys. Rev.*, 88:547–553, Nov 1952. doi: 10.1103/PhysRev.88.547. URL <https://link.aps.org/doi/10.1103/PhysRev.88.547>.
- Uwe Schumacher. Status and problems of fusion reactor development. *Naturwissenschaften*, 88(3):102–112, 2001. doi: 10.1007/s001140100214. URL <https://doi.org/10.1007/s001140100214>.
- Solar rotation as a function of depth and latitude. *Nature*, 317(6038):591–594, 1985. doi: 10.1038/317591a0. URL <https://doi.org/10.1038/317591a0>.
- Rachel Howe. Solar interior rotation and its variation. *Living Reviews in Solar Physics*, 6(1):1, 2009. doi: 10.12942/lrsp-2009-1. URL <https://doi.org/10.12942/lrsp-2009-1>.
- JR Elliott and DO Gough. Calibration of the thickness of the solar tachocline. *The Astrophysical Journal*, 516(1):475, 1999.

- TM Rogers. On limiting the thickness of the solar tachocline. *The Astrophysical Journal*, 733(1):12, 2011.
- P. A. Gilman. The tachocline and the solar dynamo. *Astronomische Nachrichten*, 326(3-4):208–217, 2005. doi: <https://doi.org/10.1002/asna.200410378>. URL <https://onlinelibrary.wiley.com/doi/abs/10.1002/asna.200410378>.
- Nicholas J. Wright and Jeremy J. Drake. Solar-type dynamo behaviour in fully convective stars without a tachocline. *Nature*, 535(7613):526–528, 2016. doi: 10.1038/nature18638. URL <https://doi.org/10.1038/nature18638>.
- J. Christensen-Dalsgaard, D. O. Gough, and M. J. Thompson. The Depth of the Solar Convection Zone. *ApJ*, 378:413, September 1991. doi: 10.1086/170441.
- Jörg Schumacher and Katepalli R. Sreenivasan. Colloquium: Unusual dynamics of convection in the sun. *Rev. Mod. Phys.*, 92:041001, Oct 2020. doi: 10.1103/RevModPhys.92.041001. URL <https://link.aps.org/doi/10.1103/RevModPhys.92.041001>.
- Robert B. Leighton. The solar granulation. *Annual Review of Astronomy and Astrophysics*, 1(Volume 1, 1963):19–40, 1963. ISSN 1545-4282. doi: <https://doi.org/10.1146/annurev.aa.01.090163.000315>. URL <https://www.annualreviews.org/content/journals/10.1146/annurev.aa.01.090163.000315>.
- Alexander G Kosovichev. Advances in global and local helioseismology: an introductory review. *The Pulsations of the Sun and the Stars*, pages 3–84, 2011.
- Jørgen Christensen-Dalsgaard. Helioseismology. *Reviews of Modern Physics*, 74(4):1073, 2002.
- David Korda. *Helioseismic inversions of plasma flows and sound-speed perturbations*. PhD thesis, Univerzita Karlova, Matematicko-fyzikální fakulta, Astronomický ústav UK, Praha, 2020. Dizertační práce, vedoucí Švanda, Michal.
- Maria Pia di Mauro. A review on asteroseismology. *arXiv: Solar and Stellar Astrophysics*, 2016. URL <https://api.semanticscholar.org/CorpusID:119375156>.
- JW Harvey, F Hill, RP Hubbard, JR Kennedy, JW Leibacher, JA Pintar, PA Gilman, RW Noyes, AM Title, J Toomre, et al. The global oscillation network group (gong) project. *Science*, 272(5266):1284–1286, 1996.
- P. H. Scherrer, R. S. Bogart, R. I. Bush, J. T. Hoeksema, A. G. Kosovichev, J. Schou, W. Rosenberg, L. Springer, T. D. Tarbell, A. Title, C. J. Wolfson, I. Zayer, and MDI Engineering Team. The Solar Oscillations Investigation - Michelson Doppler Imager. *Sol. Phys.*, 162(1-2):129–188, December 1995. doi: 10.1007/BF00733429.
- HMI. Helioseismic and Magnetic Imager for SDO, 2010. URL <http://hmi.stanford.edu/>.

- Pesnell, D. and Patel A. SDO |Solar Dynamics Observatory, 2020. URL <https://sdo.gsfc.nasa.gov/>.
- W. Dean Pesnell, B. J. Thompson, and P. C. Chamberlin. The Solar Dynamics Observatory (SDO). *Sol. Phys.*, 275(1-2):3–15, January 2012. doi: 10.1007/s11207-011-9841-3.
- Sami K Solanki, JC del Toro Iniesta, Joachim Woch, A Gandorfer, Johann Hirzberger, A Alvarez-Herrero, T Appourchaux, V Martínez Pillet, I Pérez-Grande, E Sanchis Kilders, et al. The polarimetric and helioseismic imager on solar orbiter. *Astronomy & Astrophysics*, 642:A11, 2020.
- Chunhui Xu, Jason T. L. Wang, Haimin Wang, Haodi Jiang, Qin Li, Yasser Abdulllah, and Yan Xu. Super-resolution of soho/mdo magnetograms of solar active regions using sdo/hmi data and an attention-aided convolutional neural network. *Solar Physics*, 299(3):36, 2024. doi: 10.1007/s11207-024-02283-1. URL <https://doi.org/10.1007/s11207-024-02283-1>.
- Laurent Gizon and Aaron C Birch. Local helioseismology. *Living Reviews in Solar Physics*, 2:1–131, 2005.
- S Couvidat and AC Birch. Optimal gaussian phase-speed filters in time-distance helioseismology. *Solar Physics*, 237:229–243, 2006.
- Laurent Gizon, Aaron C Birch, and Henk C Spruit. Local helioseismology: three-dimensional imaging of the solar interior. *Annual Review of Astronomy and Astrophysics*, 48:289–338, 2010.
- Jr. Duvall, T. L., S. M. Jefferies, J. W. Harvey, and M. A. Pomerantz. Time-distance helioseismology. *Nature*, 362(6419):430–432, April 1993. doi: 10.1038/362430a0.
- Li Zhao and Thomas H. Jordan. Sensitivity of frequency-dependent traveltimes to laterally heterogeneous, anisotropic Earth structure. *Geophysical Journal International*, 133(3):683–704, June 1998. doi: 10.1046/j.1365-246X.1998.00524.x.
- Laurent Gizon and AC Birch. Time-distance helioseismology: the forward problem for random distributed sources. *The Astrophysical Journal*, 571(2):966, 2002.
- Laurent Gizon and AC Birch. Time-distance helioseismology: noise estimation. *The Astrophysical Journal*, 614(1):472, 2004.
- D. Lynden-Bell and J. P. Ostriker. On the stability of differentially rotating bodies. *MNRAS*, 136:293, January 1967. doi: 10.1093/mnras/136.3.293.
- A. G. Kosovichev and T. L. Duvall. *Acoustic Tomography of Solar Convective Flows And Structures*, pages 241–260. Springer Netherlands, Dordrecht, 1997. ISBN 978-94-011-5167-2. doi: 10.1007/978-94-011-5167-2_26. URL https://doi.org/10.1007/978-94-011-5167-2_26.
- A. C. Birch and A. G. Kosovichev. Travel Time Sensitivity Kernels. *Sol. Phys.*, 192:193–201, March 2000. doi: 10.1023/A:1005283526062.

- Raymond Burston, Laurent Gizon, and Aaron C. Birch. Interpretation of Helioseismic Travel Times. Sensitivity to Sound Speed, Pressure, Density, and Flows. *Space Sci. Rev.*, 196(1-4):201–219, December 2015. doi: 10.1007/s11214-015-0136-0.
- John Parr Snyder and Philip M Voxland. *An album of map projections*. Number 1453. US Government Printing Office, 1989.
- John P Snyder. *Flattening the earth: two thousand years of map projections*. University of Chicago Press, 1997.
- Neacsu M. Map Projections - A Working Manual |Eu, Mircea, 2024. URL <https://neacsu.net/docs/geodesy/snyder/>.
- JSOC. Joint Science Operations Center (JSOC) Data Products. URL <http://jsoc.stanford.edu/>.
- Sarbani Basu and HM Antia. Changes in solar rotation over two solar cycles. *The Astrophysical Journal*, 883(1):93, 2019.
- KJ Li, XJ Shi, JL Xie, PX Gao, HF Liang, LS Zhan, and W Feng. Solar-cycle-related variation of solar differential rotation. *Monthly Notices of the Royal Astronomical Society*, 433(1):521–527, 2013.
- AV Mordvinov and LA Plyusnina. Cyclic changes in solar rotation inferred from temporal changes in the mean magnetic field. *Solar Physics*, 197:1–9, 2000.
- John Robert Taylor and William Thompson. *An introduction to error analysis: the study of uncertainties in physical measurements*, volume 2. Springer, 1982.
- Karl Pearson. Note on Regression and Inheritance in the Case of Two Parents. *Proceedings of the Royal Society of London Series I*, 58:240–242, January 1895.
- Michal Švanda. Issues with time-distance inversions for supergranular flows. *A&A*, 575:A122, March 2015. doi: 10.1051/0004-6361/201425203.
- K. DeGrave and J. Jackiewicz. Helioseismic Investigation of Modeled and Observed Supergranule Structure. *Sol. Phys.*, 290(6):1547–1568, June 2015. doi: 10.1007/s11207-015-0693-0.
- François Rincon and Michel Rieutord. The Sun’s supergranulation. *Living Reviews in Solar Physics*, 15(1):6, September 2018. doi: 10.1007/s41116-018-0013-5.
- M. Švanda, M. Klvaňa, and M. Sobotka. Large-scale horizontal flows in the solar photosphere. I. Method and tests on synthetic data. *A&A*, 458(1):301–306, October 2006. doi: 10.1051/0004-6361:20054124.
- Laurence J. November. Measurement of geometric distortion in a turbulent atmosphere. *Appl. Opt.*, 25(3):392–397, February 1986. doi: 10.1364/AO.25.000392.
- Kyle DeGrave, Jason Jackiewicz, and Matthias Rempel. Validating time–distance helioseismology with realistic quiet-sun simulations. *The Astrophysical Journal*, 788(2):127, 2014.

List of Figures

1.1	The interior structure of the Sun. Credit: Wikipedia Commons/kelvinsong	4
1.2	Closeup image of granulation in solar photosphere. Credit: NSO (nso.edu).	6
2.1	An illustration of a propagation of p modes (left) and g modes (right) in the Sun's interior. Credit: di Mauro (2016).	11
2.2	Comparison of line-of-sight magnetograms taken by SOHO/MDI (left) and SDO/HMI (right). Both images were captured at 00:00:00 UT on 1 May 2010. Credit: Xu et al. (2024).	12
2.3	A power spectrum created from observations from SDO/HMI. The surface gravity wave (f mode) and sound waves (p modes) are labeled in the plot together with the resonance signal created by convection. The strong resonance present at $\nu \approx 3$ mHz for low k is the five-minute oscillation discovered by Leighton (1963).	14
2.4	A power spectrum with shown ridge filters (full line) and phase speed filters (dashed line).	14
3.1	A ring diagram created from a power spectrum of a 24 h observation by SDO/HMI at a constant frequency $\nu = 4$ mHz.	16
3.2	(a) Measured cross-covariance function for SDO/MDI medium-degree data as a function of separation distance and time lag. Positive values are white; negative values are black. The observation duration is $T = 144$ days starting in May 1996. (b) Example ray paths for acoustic wavepackets. In both a and b, the blue lines correspond to single-skip ray paths, the red lines are for two-skip ray paths, and the green lines are for three-skip ray paths. Credit: Gizon et al. (2010).	17
5.1	An image of SDO spacecraft with the main instruments HMI, AIA and EVE highlighted. Credit: NASA SDO (sdo.gsfc.nasa.gov).	25
5.2	A Dopplergram from 04/15/2024 acquired by SDO/HMI. Credit: NASA SDO (sdo.gsfc.nasa.gov).	28
5.3	Azimuthal equidistant (Postel) projection centered in Earth's north pole (right) and a distortion map of the projection (left). Credit: Snyder and Voxland (1989).	29
5.4	High-level flowchart of the folder preparation pipeline. It contains two nested iterations; the outer one over all provided DRMS requests and the inner one over all randomly sampled injected velocities.	31
5.5	A high-level flowchart of the data download pipeline. It serves as an optional middle step between the folder preparation pipeline and the tracking pipeline in cases where not all Dopplergrams are present on the local storage.	32

5.6	Left: HMI Dopplergram in helioprojective coordinates with the area of selection highlighted in green. Right: Selected area in Carrington and Stonyhurst coordinates after application of the Postel projection.	34
5.7	High-level flowchart of the tracking pipeline. It lists all FITS files (containing Dopplergrams) present in the provided folder path, sorted by date encoded in their name, and iterates over them. In each iteration a shift, determined by the injected velocity and time difference between the frame and central frame, is applied to the origin; tracked area is selected and the Postel projection is applied on it. Further, NaN values are replaced by a median of all values and quadratic surface is subtracted from the data, removing the effect of solar rotation. The processed frame is appended to a datacube array. After the iteration is complete, the datacube array is stored in a new FITS file.	35
6.1	Mean travel-time perturbation around center vs. injected velocity plots created from the dataset with the latitude of the tracked area origin equal to 0° and the following configurations: f mode, e-w geometry, $\Delta = 10$ px (top); p3 mode, e-w geometry, $\Delta = 15$ px (middle); td11 (phase speed filter), e-w geometry, $\Delta = 46$ px (bottom).	41
6.2	Mean travel-time perturbation around center vs. injected velocity plots created from a single observation date, 01/20/2019, tracked area origin latitude equal to 0° and the following configurations: f mode, e-w geometry, $\Delta = 10$ px (top); p3 mode, e-w geometry, $\Delta = 15$ px (middle); td4 (phase speed filter), e-w geometry, $\Delta = 9.9$ px (bottom).	43
6.3	Mean travel-time perturbation around center vs. injected velocity plots created from a single observation date, 01/20/2019, for the configuration: f mode, e-w geometry, $\Delta = 10$ px. The difference in configurations was the tracked area origin latitude: 0° (top), -20° (middle), 20° (bottom).	45
6.4	Mean travel-time perturbation around center vs. injected velocity plots created from a single observation date, 01/20/2019, for the configuration: p3 mode, e-w geometry, $\Delta = 15$ px. The difference in configurations was the tracked area origin latitude: 0° (top), -20° (middle), 20° (bottom).	46
6.5	Mean travel-time perturbation around center vs. injected velocity plots created from a single observation date, 01/20/2019, for the configuration: td4 (phase speed filter), e-w geometry, $\Delta = 9.9$ px. The difference in configurations was the tracked area origin latitude: 0° (top), -20° (middle), 20° (bottom).	47

6.6	Volume integrals of velocity perturbation kernels obtained from linear regression slopes (model independent) vs. volume integrals of the velocity perturbation kernels calculated from forward modelling. The data were obtained from the dataset containing 8 observation dates with the origin latitude of the tracked area equal to 0° for various ridge and phase speed filters.	48
6.7	Volume integrals of velocity perturbation kernels obtained from linear regression slopes (model independent) vs. volume integrals of the velocity perturbation kernels calculated from forward modelling. The data were obtained from the dataset containing 8 observation dates with the origin latitude of the tracked area equal to 0° for various ridge and phase speed filter groups.	49
6.8	Volume integrals of velocity perturbation kernels obtained from linear regression slopes (model independent) vs. volume integrals of the velocity perturbation kernels calculated from models. The data were obtained from the dataset containing 8 observation dates with the origin latitude of the tracked area equal to -20° (top) and 20° (bottom) for various ridge and phase speed filter groups. . . .	50
7.1	Ring diagrams created from power spectra of a 24-hour observation at $\nu = 4$ mHz. The upper diagram corresponds to a dataset with no injected velocity resulting in all rings being concentric circles. The bottom diagram was created from a dataset with an injected horizontal velocity $v_0 = 500$ m/s resulting in the visible horizontal distortion of the rings.	52
7.2	Comparison of the implanted velocity and the horizontal velocity determined from the manipulated datacubes using a LCT algorithm. . . .	53

List of Tables

- 6.1 Dopplergram configurations utilized in this thesis. T represents the observation time in hours, while ΔT denotes the cadence (the time between two consecutive frames) in seconds. Origin lon./lat. are Carrington coordinates of the projection origin of the middle frame in the sequence. The number of datacubes corresponding to the provided Dopplergram sequence (# datacubes) is determined by the number of injected velocities for the given configuration. . 38

List of Abbreviations

AIA - Atmospheric Imaging Assembly

DRMS - Data Record Management System

EVE - Extreme Ultraviolet Variability Experiment

FITS - Flexible Image Transport System

GB02 - A method of travel time calculation presented by Gizon and Birch (2002)

GB04 - A method of travel time calculation presented by Gizon and Birch (2004)

GONG - Global Oscillation Network Group

HMI - Helioseismic and Magnetic Imager

JSOC - Joint Science Operations Center

MDI - Michelson Doppler Imager

PHI - Polarimetric and Helioseismic Imager

SDO - Solar Dynamics Observatory

SOHO - Solar and Heliospheric Observatory